



HAL
open science

Assessment of the Evolution Equation Modelling approach for three-dimensional expanding wrinkled premixed flames

Eric Albin, Yves d'Angelo

► **To cite this version:**

Eric Albin, Yves d'Angelo. Assessment of the Evolution Equation Modelling approach for three-dimensional expanding wrinkled premixed flames. *Combustion and Flame*, 2012, 159 (5), pp.1932–1948. 10.1016/j.combustflame.2011.12.019 . hal-00967136

HAL Id: hal-00967136

<https://hal.science/hal-00967136>

Submitted on 28 Mar 2014

HAL is a multi-disciplinary open access archive for the deposit and dissemination of scientific research documents, whether they are published or not. The documents may come from teaching and research institutions in France or abroad, or from public or private research centers.

L'archive ouverte pluridisciplinaire **HAL**, est destinée au dépôt et à la diffusion de documents scientifiques de niveau recherche, publiés ou non, émanant des établissements d'enseignement et de recherche français ou étrangers, des laboratoires publics ou privés.

Assessment of EEM approach for 3D expanding wrinkled premixed flames

Eric Albin & Yves D'Angelo

CORIA/INSA UMR 6614 CNRS,
Avenue de l'Université 76801 St-Etienne du Rouvray, Rouen, France

Abstract

Direct Numerical Simulations (DNS), Evolution Equation Modelling (EEM) and Experimental results from the literature (EXP) are presented and analyzed for an expanding propane/air flame. DNS results are obtained thanks to the in-house finite-difference code HALLEGRO. Computed (DNS/EEM) and measured (EXP) equivalent radii R_P and R_S , mean stretch k and consumption velocity S_C , as well as sample front shapes, are compared using the same post-processing methodology. Small perturbations in the EEM input parameters induce comparatively small shifts in the compared results, showing the robustness of the approach. When slightly adapting only one $O(1)$ parameter for the EEM strategy (the effective turbulent forcing amplitude felt by the flame), DNS and EEM show quite fair agreement one with the other and also with EXP, except for one of the experiments at early times. In the context of expanding flames, this validated EEM methodology can constitute a reliable tool to compute realistically large sized flames.

Keywords: Expanding premixed flames, Evolution equation Modelling, Direct Numerical Simulation

1. Introduction

Expanding flames constitute a basic fundamental configuration for pre-mixed laminar and turbulent gaseous combustion. They have been (and are still) extensively studied under varying conditions (pressure, temperature, fuel, Lewis number...) both experimentally and numerically, for instance to determine laminar flame velocities and/or Markstein lengths (see e.g. [1] or [2]).

In many practical applications, turbulent pre-mixed flames can be considered as a collection of locally laminar flames: the flamelet regime [3], where turbulence does not substantially modify the internal structure of the laminar flame. Furthermore, for sufficiently moderate turbulence, the flame is only wrinkled and the turbulent expanding flame front can be considered as a slightly deformed ("wrinkled" or "corrugated") sphere.

In [4], turbulent 3D expanding air/methane, air/propane and air/hydrogen flames are measured at atmospheric pressure. An internal combustion engine-like configuration, with an optically accessible cylindrical combustion chamber has also been considered in [5, 6, 7]. Reference [8] (which results will also be compared with those of present paper) is interested in the dynamics of an expanding propane/air flame, again in an engine-like configuration.

To investigate the expanding flame behaviour, one can numerically solve the full set of 3D Navier-Stokes reactive equations (see for instance [9, 10, 11] or the recent work [12]). However, for realistically large sizes, and because of the very small spatio-temporal scales involved both from turbulence and chemical reaction, the required computational effort may become impractical.

Instead of using “brute force” simulations, one can try instead to take advantage of the scale separation (the flame front is very thin) and solve an evolution equation for the flame front only. Since only the flame surface needs to be parameterized, one spatial dimension is removed from the computation. Moreover, all pertinent physical parameters can be lumped into few ones; here, as this will be specified on the sequel, only three (plus one) physical parameters are needed : namely the density contrast α , the Markstein length \mathcal{L}_u , the laminar flame velocity S_0^L . To mimic turbulent flow, and since the EEM (Evolution Equation Modeling) approach does not solve for the flow, a synthetic turbulent forcing u' must also be supplied. The aim of the paper is to tentatively assess a chosen EEM strategy for 3D expanding flames (from reference [13]) by comparing its results with present DNS (Direct Numerical Simulations) and available experimental data from the literature.

For the DNS calculations, we used the in-house compressible code HALlegro while experimental results are those of [4] and [8]. These experiments were considered because i) we are mainly interested on the effect of weak ($u'/S_L \sim 1$) turbulence on the flame. ii) the configuration is quite straightforward to compute (an expanding stoichiometric propane/air flame at room pressure) ; iii) we have access to the experimental data and we can use the same post-processing strategy for our DNS results.

The paper is organized as follows. Basic definitions of the set-up and of experimental outputs, i.e. the quantities profiles that will be actually compared to the DNS and EEM computations, are introduced section 2. Section 3 presents the system of governing equations solved by the in-house code HALlegro. The DNS and EXP post-processing procedure, based on polynomial interpolation [4], and its limitations, as well as the influence of BC treatment on the shape of the computed flame, are also tested on preliminary laminar benchmarks. The numerical set-up for turbulent wrinkled flames computation is finally presented at the end of the section. The EEM approach, similar to the one from [13], is outlined section 4, as well as the adopted numerical strategy (Exponential Time Differencing Runge-Kutta method, or ETDRK, in the Fourier-Legendre basis) to solve it. The way to mimic external “turbulent” forcing by a Passot-Pouquet spectrum and a proposed equation for the mean flame radius can also be found there.

Section 5 shows comparisons and analysis of DNS/EEM/EXP results. Also included is robustness testing of the EEM strategy when slightly varying some input parameters. Concluding remarks and perspectives end the paper section 6.

2. Basic definitions, Markstein law

In this section, we introduce the basic quantities that are experimentally determined and that will be used as comparison for numerical modelling (DNS and EEM).

2.1. Basic definitions, general case

A three-dimensional spherical flame can be triggered by spark electrodes in a turbulent pre-mixture of e.g. air/propane. Experimental techniques such as PIV and laser tomography may then give access to pictures of flame surface and burnt gas production.

If the flame front is sufficiently thin, and separates burnt gas (referred to with b subscript in the sequel) from fresh (unburned) mixture (referred to with u subscript), two experimentally accessible characteristic radii, respectively denoted R_S and R_P can be introduced. They are based on burnt gas surface S (equation (1a)) and two-dimensional flame section perimeter L (equation (1b)) :

$$S = \pi R_S^2 \tag{1a}$$

$$L = 2\pi R_P \tag{1b}$$

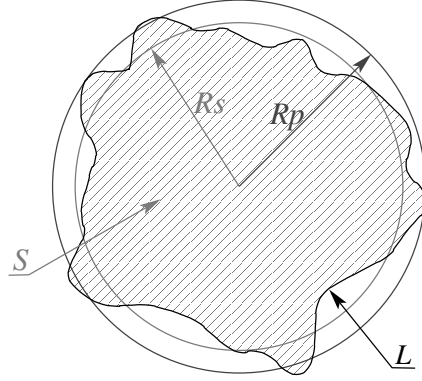


Figure 1: Experimentally determined equivalent flame radii R_S and R_P ; equations (1a) and (1b).

Figure 1 presents a typical sample contour of experimentally obtained flame surface contour. From a measured image, radius R_S can be determined by computing the number of pixels associated with burnt gas. For R_P , it is necessary to evaluate the flame length. One should first determine which pixels belong to the flame front, then smooth the contour before evaluating its length [4]. These two radii can be related to consumption speed S_C , mean turbulent flame velocity S_T (the mean displacement speed) and mean stretch k , that will be defined below.

For a cylindrical-in-average or spherical-in-average turbulent flame, the mean turbulent velocity S_T can be computed as [4, 14, 1]

$$S_T = \frac{\rho_b}{\rho_u} \frac{dR_S}{dt} = (1 - \alpha) \frac{dR_S}{dt} \quad (2)$$

where α denotes the density contrast $\alpha = \frac{\rho_u - \rho_b}{\rho_u}$. Equation (2) can be obtained by mass conservation through the (infinitely thin) flame front. The consumption rate of the fresh mixture S_C (the mean burning velocity) can similarly be expressed as

$$S_C = \frac{\rho_b}{\rho_u} \left(\frac{R_S}{R_P} \right)^\xi \frac{dR_S}{dt} \quad (3)$$

with $\xi = 1$ for cylindrical-in-average flames and $\xi = 2$ for spherical-in-average flames. Note that equation (3) assumes that the front is infinitely thin. If a non-zero (thermal) thickness l_t is assumed for the 3D front (i.e. if l_t/R_P is not $\ll 1$), another expression can be derived for S_C [15, 16]

$$S_C = \frac{\rho_b}{\rho_u} \left(\frac{R_S}{R_P} \right)^2 \frac{dR_S}{dt} \left(\frac{1}{1 + (l_t/R_P)^2} \right) \quad (4)$$

The local flame stretch κ can be defined as [17, 4, 16]

$$\kappa \equiv \frac{1}{\delta S} \frac{\partial \delta S}{\partial t} \quad (5)$$

where δS is a local element of front surface. From equation (5), one can deduce the mean flame stretch k as [18]

$$k = \frac{1}{S_u} \frac{dS_u}{dt} \quad (6)$$

with S_u the total flame front surface. It is linked to R_p according to [15, 16]

$$k = \frac{\xi}{R_p} \frac{dR_p}{dt} \quad (7)$$

with again $\xi = 1$ for cylindrical-in-average flames and $\xi = 2$ for spherical-in-average flames.

From asymptotic theory and experiments, the consumption rate S_C can be related to mean flame stretch k according to [15, 17, 16]

$$S_C = S_L^0 - \mathcal{L}_u k \quad (8)$$

where \mathcal{L}_u is a Markstein length and S_L^0 is the laminar (unstretched) flame velocity.

2.2. Laminar case

In the laminar case, for 2D and 3D expanding flames, the front is perfectly circular or spherical. Hence, the above introduced radii are identical : $R_S = R_p = R$ and the stretch k (mean or local) is equal to $k = \frac{\xi}{R} \frac{dR}{dt}$. Markstein law (8) becomes

$$\frac{dR}{dt} = \frac{S_L^0}{1 - \alpha} - \mathcal{L}_b \frac{\xi}{R} \frac{dR}{dt} \quad (9)$$

where $\mathcal{L}_b = \mathcal{L}_u/(1 - \alpha)$ denotes the ‘‘second Markstein length’’ [17]. Equation (9) can be cast in separate variables form as

$$\frac{dR}{dt} = \frac{S_L^0}{1 - \alpha} \cdot \frac{1}{1 + \xi \mathcal{L}_b/R} \quad (10)$$

This equation admits a closed form solution — the Lambert function of an exponential [19] — or may be more conveniently solved numerically. These analytical results as well as experiments from [8] will be used to validate preliminary DNS results for the laminar case, as it will be shown section 5.

3. DNS of expanding flames

3.1. Governing equations, numerical strategy, BCs

The set of governing equations are the fully compressible reactive Navier–Stokes equations, that can be cast as

$$-\frac{\partial \rho}{\partial t} = \frac{\partial \rho U_j}{\partial x_j} \quad (11)$$

$$-\frac{\partial \rho U_i}{\partial t} = \frac{\partial \rho U_i U_j}{\partial x_j} + \frac{\partial P}{\partial x_i} - \frac{\partial \tau_{ij}}{\partial x_j} \quad (12)$$

$$-\frac{\partial \rho E}{\partial t} = \frac{\partial}{\partial x_j} (U_j (P + \rho E)) - \frac{\partial}{\partial x_j} \left(\lambda \frac{\partial T}{\partial x_j} \right) - \frac{\partial \tau_{ij} U_i}{\partial x_j} - \tilde{S}_5 \quad (13)$$

$$-\frac{\partial \rho Y_k}{\partial t} = \frac{\partial \rho U_j Y_k}{\partial x_j} - \frac{\partial}{\partial x_j} \left(D \frac{\partial Y_k}{\partial x_j} \right) - \tilde{S}_k \quad (14)$$

in conservative form and with usual notations. Temperature T is deduced from total energy $\rho E = \rho C_V T + \rho U_i^2 / 2$. Pressure is computed from perfect gas law $P = \rho r T$ and power law is assumed for dynamic viscosity $\mu \sim T^{0.76}$. Heat diffusion coefficient λ and scalar conductivity D are deduced from dynamic viscosity μ by assuming fixed values of Prandtl and Schmidt numbers. The stress tensor τ_{ij} is given by its

Newtonian fluid expression (with δ_{ij} the Kronecker delta) : $\tau_{ij} = \mu \left(\frac{\partial U_i}{\partial x_j} + \frac{\partial U_j}{\partial x_i} \right) - \frac{2}{3} \mu \frac{\partial U_k}{\partial x_k} \delta_{ij}$. The terms \widetilde{S}_k and \widetilde{S}_5 represent source terms due to combustion. Chemistry is simplified assuming single step Arrhenius kinetics; pre-exponential factor is tuned with respect to local equivalence ratio in order to fit the correct value of the laminar flame velocity [20].

The DNS solver we employed is the in-house parallel solver HALlegro [21, 22]. It is based on a 6th-order compact explicit finite difference scheme, applied on hybrid collocated/staggered grids, coupled to a low-storage third-order Runge-Kutta algorithm to march in time. Within the context of the present work, the main advantages of the solver are i) increased robustness, compared with a pure collocated strategy, i.e. the possibility of using coarser grids while preserving the same accuracy; ii) the unambiguous definition of boundary points, compared with a pure staggered strategy, allowing for straightforward acoustic outflow BC treatment. For the expanding flames we computed, non reflecting outflow treatment of [23] demonstrated robustness and very low influence on flame shape, while the non-reflecting strategy of [24] makes the flame become square, as will be shown figure 3a.

3.2. Laminar case, post-processing

To ensure a coherent comparison between numerical and experimental results, we made use of the same post-processing procedure — in particular the same interpolation (smoothing) procedure for determining the flame front — as the one used in [4, 15]. We shall evidence in this subsection some experimental and numerical shortcomings : on the one hand, the post-processing interpolation procedure does not allow to correctly capture the flame front under a 2 mm radius; on the other hand, the numerical boundary condition treatment (the popular NSCBC and 3D-NSCBC) may induce a square-shaped front when approaching the outflow boundaries.

We hence tested the procedure on laminar flames, both for cylindrical and spherical fronts. We performed three computations : i) a cylindrical flame with usual NSCBC outlets [24], ii) a cylindrical flame with 3DNSCBC outlets [23, 25], iii) a spherical 3D flame with 3DNSCBC. Since we would like to test the present procedure mainly for the turbulent case, we do not exploit any symmetries in the computations. The mixture is ignited by forcing at initial time a Gaussian profile for temperature and composition at the center of the computational domain.

Figure 2 represents temperature contours for each of these three cases. The points (\sim pixels, for a corresponding measurement) where T (in Kelvins) stands in the interval [1076; 1223] are reproduced as +. The used smoothing procedure [4] consists in polynomial interpolation to determine the R_p radius.

At initial time $t = 0$, figure 2 shows a significant discrepancy between the simulated front and the smoothed front. At small radii, the flame front is not sufficiently resolved (too few points/pixels to mark it) and it seems that at these early times the smoothing procedure is not able to find a suitable front shape and position. At larger times and radii, the resolution is sufficient and the value of R_p reliable. From these preliminary results, and as in the experiments [4], we considered that the front shape and position was correctly captured by the smoothing procedure only above a radius value of 2 mm.

Figure 3 presents ten equally spaced (in time) contours for the three aforementioned configurations. For cylindrical flames, the flame radius increases at a constant rate as shown in figure 3b. In the spherical case, figure 3c shows that the flame speed tends to increase with time.

Figure 4 shows flame radius time evolution $R(t)$ for CH_4 /air laminar flames in the 2D and 3D expanding cases. As expected, in this laminar case, the two computed radii R_S and R_p were found numerically equal to R . For the three computational cases (2D with NSCBC or 3DNSCBC, 3D with 3DNSCBC), we plot the computed radius against experimental results from [4] and [8]. From equations (2), (3) and (7), we can compute consumption velocity S_C , mean velocity S_T and stretch k . Time evolutions for S_C , S_T and k are shown figure 5 and as a function of $R(\equiv R_S \equiv R_p)$ figure 6.

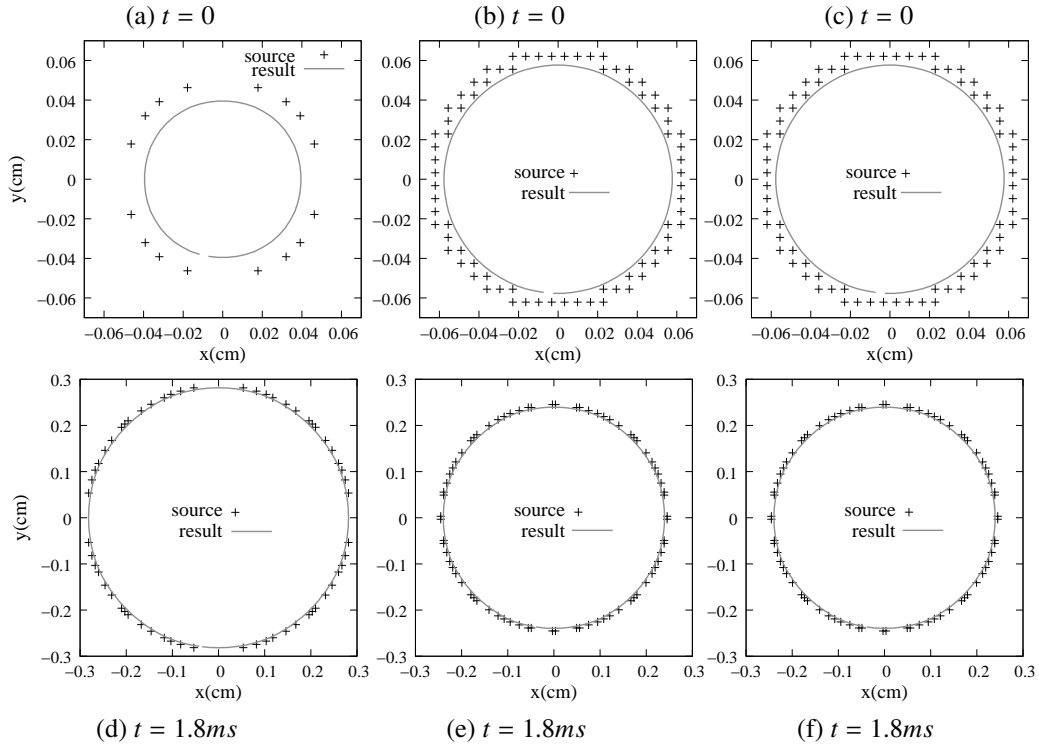


Figure 2: Radii R_P and R_S determination by front flame smoothing (same procedure as in [15]) : (a,d) cylindrical flame with NSCBC outlets ; (b,e) cylindrical flame with 3D-NSCBC outlets [23, 25], (c,f) spherical flame with 3D-NSCBC outlets (equatorial section). Only above 2 mm is the flame front correctly resolved.

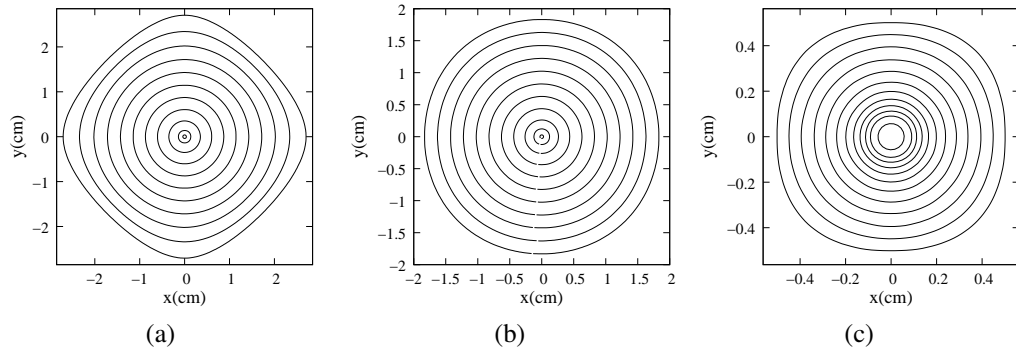


Figure 3: Temperature iso-contours time evolutions : (a) cylindrical flame with NSCBC outlets in a $5.7 \times 5.7 \text{ cm}^2$ computational domain (800^2 grid points), $\Delta t = 1.05 \text{ ms}$. (b) $(4 \text{ cm})^2$ (600^2 grid points), cylindrical flame with 3D-NSCBC outlets in a $\Delta t = 0.789 \text{ ms}$. (c) spherical flame sections with 3DNSCBC outlets in a $(1.125 \text{ cm})^3$ computational domain, $\Delta t = 0.3 \text{ ms}$

Figure 7 shows consumption velocity S_C as a function of k . Again, all these computed quantities are compared with experimental results from [4] and [8].

As expected [4], flame radius increases faster in the cylindrical configuration and the influence of bound-

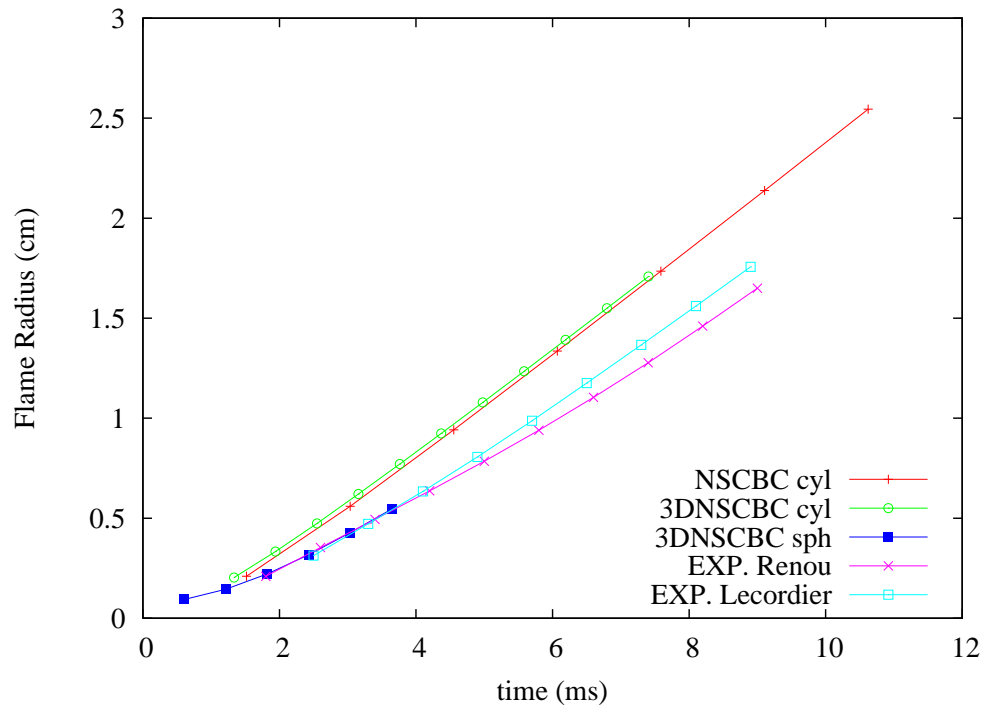


Figure 4: Time evolution of flame radius R for computed CH_4 /air 2D and 3D laminar expanding flames, with NSCBC and 3DNSCBC outflow boundary condition treatment. Experimental points are those of Renou [4] and Lecordier [8].

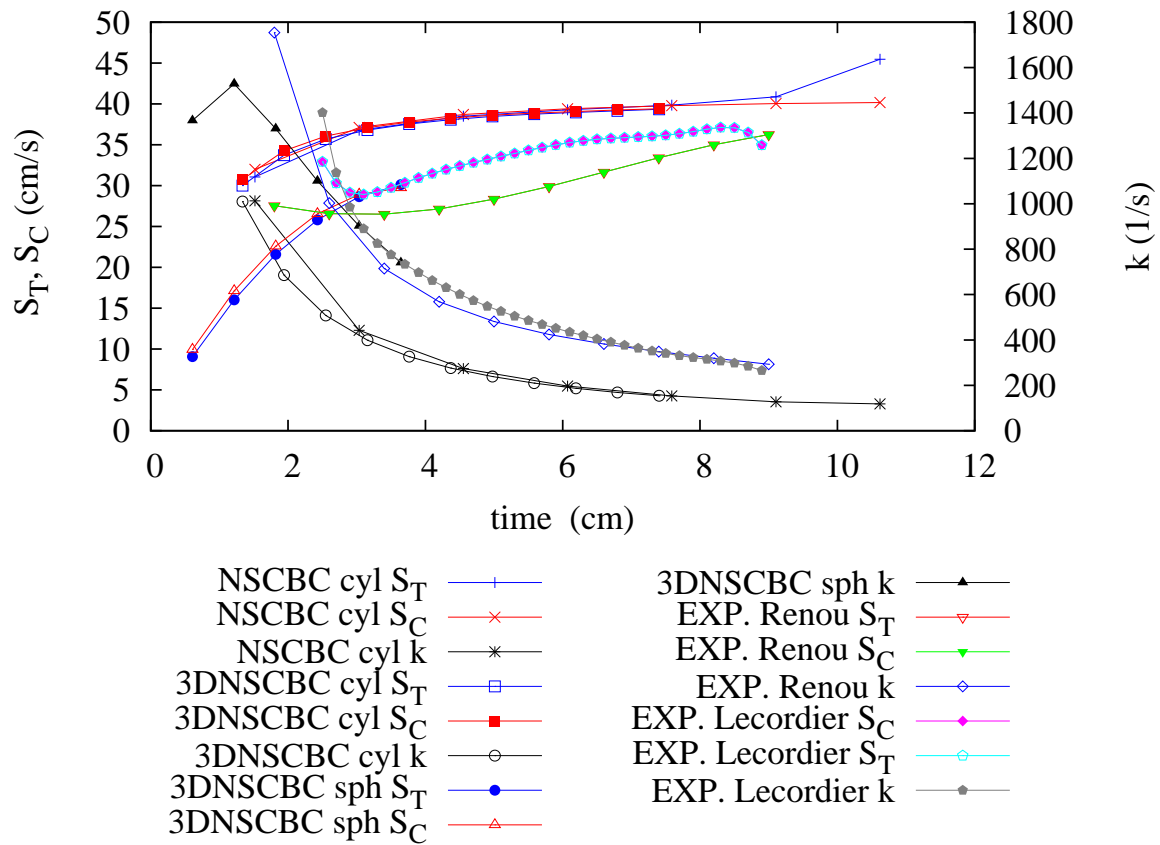


Figure 5: Time evolution of mean velocity S_T , consumption speed S_C and stretch k for computed CH_4 /air 2D and 3D laminar expanding flames. As in figure 4, experimental points are those of Renou [4] and Lecordier [8].

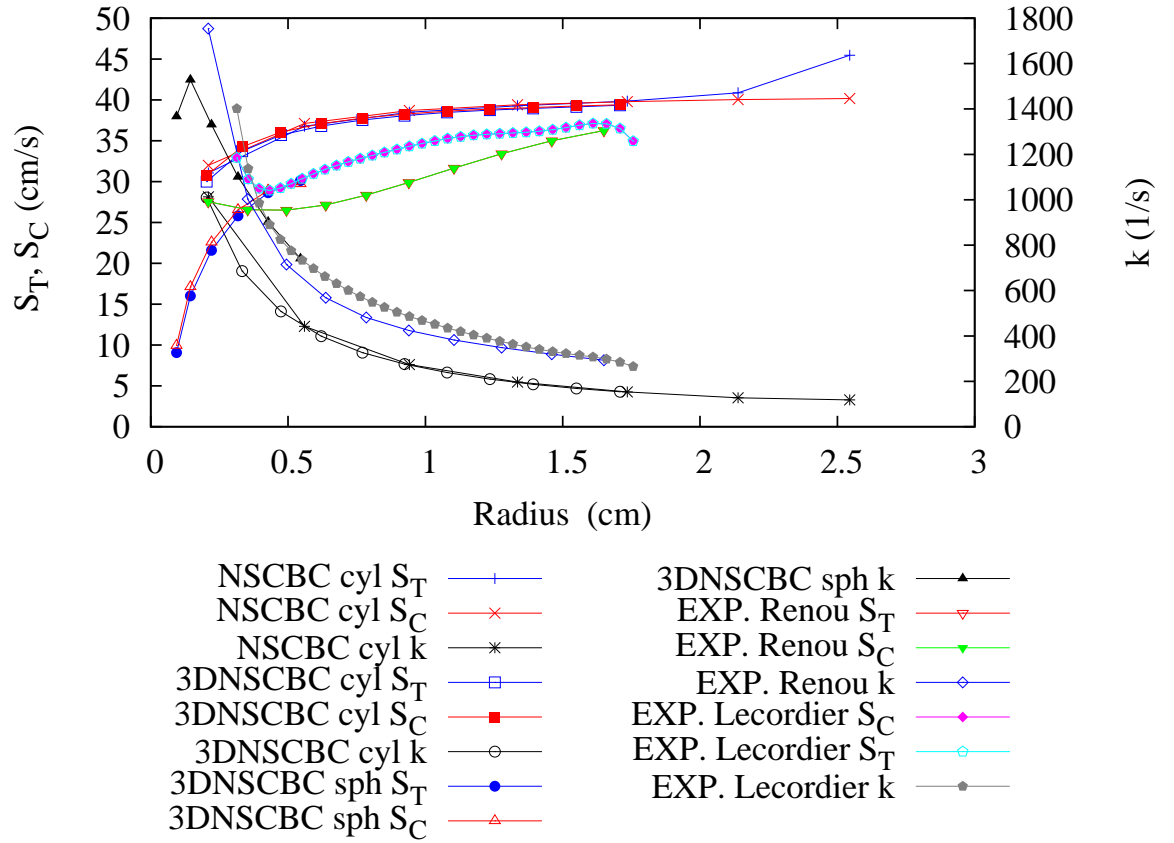


Figure 6: Evolution of mean velocity S_T , consumption speed S_C and stretch k as a function of flame radius for computed CH_4 /air 2D and 3D laminar expanding flames. Same comparisons as in figure 5.

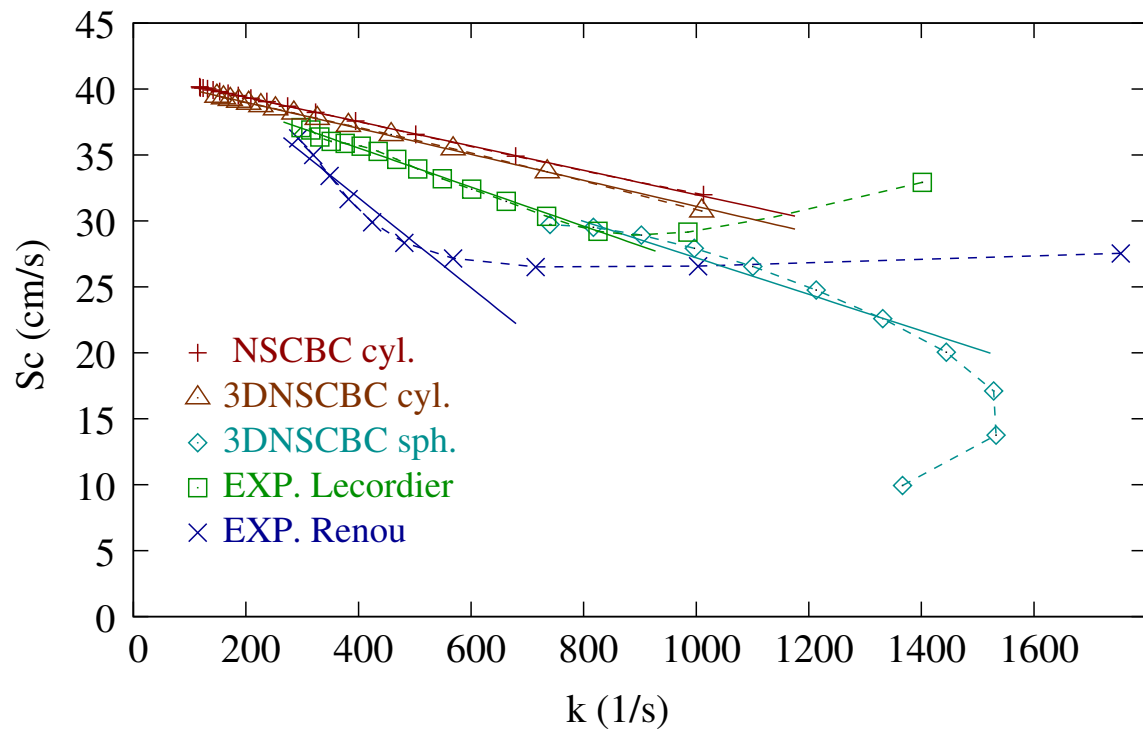


Figure 7: Evolution of consumption velocity S_C as a function of stretch k for computed CH_4/air 2D and 3D laminar expanding flames. Same comparisons as in figure 4. Solid lines are Markstein law representations (eq. (8)) with different Markstein lengths.

ary condition treatment remains small. In the cylindrical case, the flame consumption velocity tends quite quickly to its limit (planar) value $S_L^0 = 0.407m/s$, while in the spherical case S_C stays at a lesser level during the evolution, as also noticed experimentally in [4] and [8].

Very good agreement is obtained between DNS results of the spherical case and experimental results from [8], as is the observed trend for larger radii. However, results from [4], even if compatible at large times/radii, do not as fairly match neither DNS nor results from [8]. Estimation of S_C or k is very sensitive to the smoothing procedure used to compute dR/dt from raw data [19] and also to measurement frequency. This may be the main cause of the observed discrepancies. Another possible source of inaccuracy at early times may rely in the ignition device (PRECISER LES DIFFERENCES entre les deux since reference XXX made use of while reference YYY employed

Figure 7 shows that consumption velocity is an affine function of stretch k . However, a short transient is observed before Markstein law is verified (cf. large values of k , i.e. small values of radius or time). This may be due to our Gaussian initialization procedure used for initiating the DNS. Notice that this transient is shorter in the DNS than in the experiments. Table 1 reports the best fits of laminar velocity S_L^0 and first Markstein length \mathcal{L}_u obtained to match Markstein law (8) (the straight lines in figure 7.) By extrapolation

Configuration	$S_L^0(cm/s)$	$\mathcal{L}_u(\mu m)$
Cylindrical, NSCBC	41.22	92.3
Cylindrical, 3DNSCBC	40.96	98.5
Spherical, 3DNSCBC	41.02	138
Experimental, spherical, from ref. [8]	41.46	148
Experimental, spherical, from ref. [4]	45.40	341

Table 1: Laminar flame velocity S_L^0 and first Markstein length \mathcal{L}_u for computed and measured expanding flames.

to zero stretch, DNS give a value of S_C close to less than 1% from the expected value of $S_L^0 = 0.407m.s^{-1}$. While experiments from [8] are at less than 2% from this value, measurements from [4] are around 12%. Also notice that the obtained slope (i.e. the Markstein length \mathcal{L}_u) from DNS is fully compatible with experiments from [8] (138 vs. 148 μm). As expected [17], the computed values from the cylindrical case perceptibly differ from the one obtained in the cylindrical case.

This preliminary computations in the laminar case allowed us to validate the adopted computational strategy to simulate the expanding front. We are now ready to compute turbulent expanding flames.

3.3. DNS of turbulent wrinkled flames

In [11], a 3D expanding flame was computed in a $(5\text{ mm})^3$ cube, with a 128^3 equally spaced grid. The employed numerical method was based on a finite-difference collocated Padé scheme for space derivative and third-order Runge-Kutta scheme in time. To save CPU resources, single-step chemistry was used. Resulting spatial resolution was around $40\mu m$. Since our in-house code HALlegro is essentially staggered (except at the boundaries), we were able to use a spatial grid size of around $60\mu m$, corresponding — thank to the hybrid collocated/staggered arrangement [22] — to an equivalent (effective) size of less than $40\mu m$. Our grid consisted in 480^3 nodes for a physical domain of $(30\text{ mm})^3$. In preliminary 1D and 2D tests, this spatial resolution was sufficient to retrieve a correct value of the laminar flame velocity from the computations [21]

In the present study, we consider a stoichiometric air/propane pre-mixture and we wish to impose a 3-mm integral length and an initial turbulent intensity of $u'/S_L = 0.8$ (u' being the rms value of turbulent velocity fluctuations). To this aim, we first generate a Passot-Pouquet [26] spectrum on a smaller 240^3

grid, corresponding to 1/8 of the total computational domain (the choice of a smaller grid was induced by computational resource constraints). Figure 8a shows this “1/8” grid, an iso-level of the initial velocity field $|\mathbf{u}| = u'$, colored by vorticity modulus. This grid is duplicated in order to fill in the whole computational domain (see figure 8b). This initial condition freely evolves through code iterations during 1.2 *ms* with periodic boundary conditions, in order to obtain an acceptable approximation of decaying homogeneous isotropic turbulence [21]. The boundary conditions are then changed to 3DNSCBC acoustic outflows. As in the laminar case, the pre-mixture is ignited in the center thanks to a Gaussian profile in temperature and composition (cf. figure 8c). Flame expansion is computed until a physical time of 7.28 *ms* is reached. Total CPU cost was 70 000 hours on 512 4.7 GHz processors. Figures 9a to 10h represents iso-contours of reaction rate during flame expansion. Vorticity iso-levels are also presented.

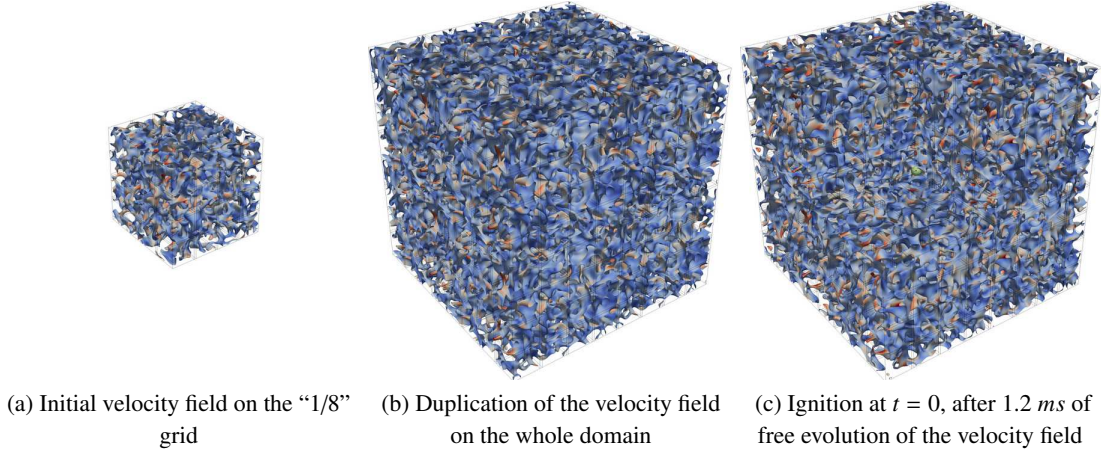


Figure 8: Initialization procedure (before ignition) for a propane/air stoichiometric 3D expanding flame.

Notice that, due to not high enough initial values of outflowing velocities, negative velocities can appear at the outlets and spurious oscillations were indeed obtained at the outlets after 3.16 *ms*. A local filtering procedure was used to temporarily damp turbulence at the outflows and stabilize the computation. This local filtering does not seem to significantly affect flame/turbulence interaction during front expansion, as also confirmed by preliminary 2D tests [21].

To perform the analysis of this simulation, we realize three sections of temperature iso-levels (at 500 K VERIFIER AVEC ERIC XXXX), corresponding to the coordinates plans xOy , xOz and yOz , and monitor their time evolution on figures 11a, 11b and 11c. We can observe that the contours are much closely packed near the ignition kernel. Early flame velocities are small, as expected, due to large curvature of initial front. For post-processing, we again made use of the same methodology employed for the laminar case (section 3.2) and experiments from [4]. Results presentation — determination of equivalent radii R_P and R_S , consumption velocity S_C , mean turbulent speed S_T and average stretch k — and analysis is post-poned section 5 to compare it with the Evolution Equation Modelling (EEM) strategy presented next section and experimental results.

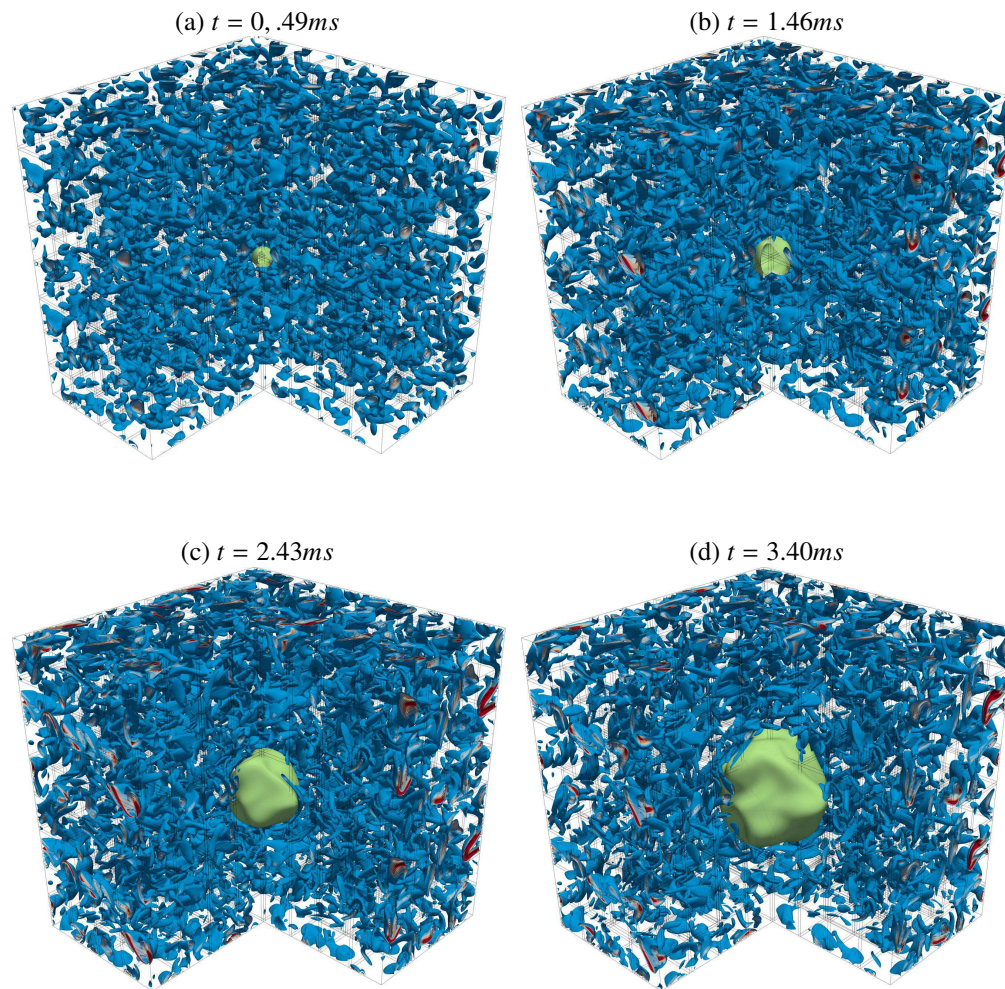


Figure 9: Three dimensional simulation of a propane/air stoichiometric expanding flame. Iso-contours of vorticity (blue to red) and of reaction rate (green). Physical times shown range from 0.49 to 3.40 *ms* (continued in figure 10).

4. EEM strategy

The Evolution Equation Modeling (EEM) approach consists in building (and solving) an equation for the flame surface dynamics only, and not computing the 3D reactive flow. Of course, since it does not solve for turbulence nor flame/turbulence interaction, it cannot replace the full 3D reactive equations. It is therefore limited to simple geometrical configurations. However, in the present context of 3D spherical-in-average expanding flame, we wish here to solve for a simple equation, adjust only one parameter and try to provide pertinent information on flame dynamics.

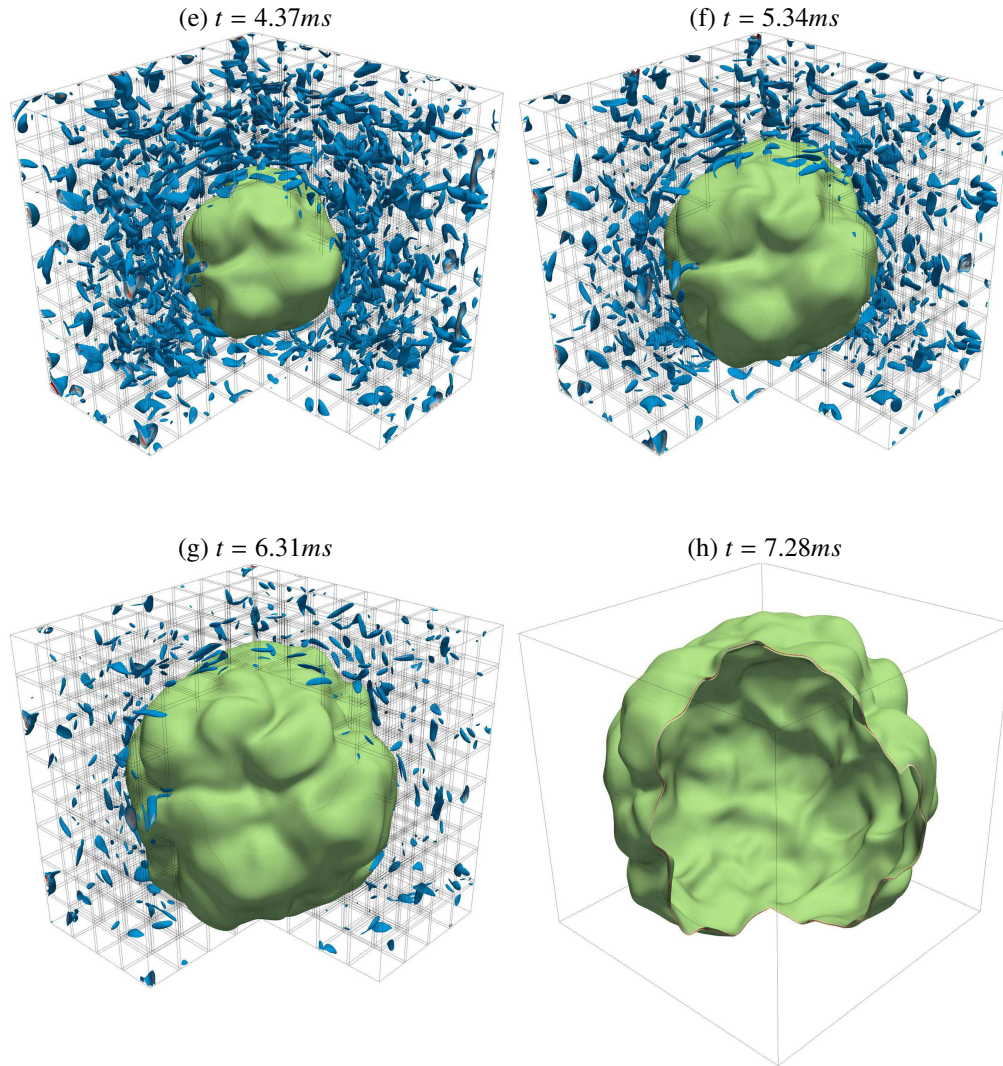


Figure 10: Three dimensional simulation of a propane/air stoichiometric expanding flame. Iso-contours of vorticity (blue to red) and of reaction rate (green). Physical times range here from 4.37 to 7.28 *ms*.

4.1. Chosen Evolution Equation

In [27], it was shown that the unburned to burnt density contrast¹ $\alpha \equiv (\rho_u - \rho_b)/\rho_u$ may be used as expansion parameter to derive evolution equations. In this perturbative approach, if $\alpha \ll 1$, the Landau–Darrieus hydrodynamic instability mechanism of spontaneous wrinkling is weak. Reference [27] was the first to propose a leading–order, weakly non-linear equation for flame shape dynamics : the so-called Michelson–

¹Notice that $0 < \alpha < 1$. This parameter naturally appears in the governing equations and has already been introduced section 2.1.

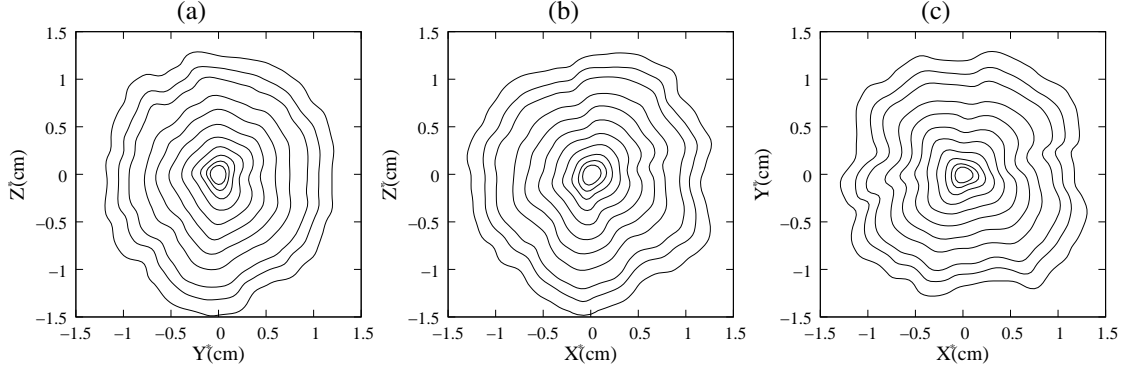


Figure 11: DNS of an expanding flame : sections of iso-levels of temperature as a function of time. Each contour is separated by a time step of 0.6 ms .

Sivashinsky (MS) equation, or more simply Sivashinsky equation. Since then, many other attempts and techniques to improve this equation or to propose other kinds of EEM equations can be found in the literature : e.g. higher order expansions in α for MS type equations [28, 29, 30], second order in time equations for transients or acoustics [31, 32] non perturbative approaches [33, 34], asymptotic expansion based on flame aspect ratio [35], 3D planar equations [36, 37, 38], equations dealing with non connected or non stellate front topology [39, 40, 41].

In the context of 3D expanding flames [13, 42, 43], many of the proposed equations can be seen as different extensions of Michelson–Sivashinsky equation. For reasons specified later on, the chosen asymptotic EE is the one proposed and analysed in [13]. It reads

$$\frac{1}{S_L^0} \frac{\partial \mathcal{F}}{\partial t} = \Omega(\alpha) \left(\frac{H(\mathcal{F})}{R_M} - \frac{1}{K_n} \frac{C(\mathcal{F})}{R_M^2} \right) + a(\alpha) \frac{\|\nabla_S \mathcal{F}\|^2}{2R_M^2} + \text{CT} + u' \quad (15)$$

$\mathcal{F}(\mathcal{R}, \theta, \varphi) = \mathcal{R} - R_M$ denotes the front deformation (in spherical coordinates, θ the co-latitude and φ the longitude), \mathcal{R} is the instantaneous flame radius (depending on t , θ , and φ), R_M is the mean flame radius, so that at any time the mean value of \mathcal{F} on the sphere is zero. This equation has a Michelson-Sivashinsky like structure and each term can be physically interpreted :

- i) The operator $H(\cdot)$ and $C(\cdot)$ are respectively the “hydrodynamic” and “curvature” operators : they are linear and diagonal in the Fourier-Legendre basis (see below); H represents the contribution of the Landau-Darrieus instability, due to streamlines deflection; C accounts for the influence of front local curvature on local burning velocity. The used expressions in present work are given (in the Fourier-Legendre basis) equations (22 –23).

While H has essentially no reference scale [29], C introduces a reference length, $\sim 1/K_n$, with K_n the neutral wavenumber, linked to Markstein length, [29].

- ii) The symbol ∇_S denotes the surface gradient $\nabla_S(\cdot) \equiv (\partial(\cdot)/\partial\theta, 1/\sin\theta\partial(\cdot)/\partial\varphi)$. This term in the RHS of equation (15) corresponds to the Huygens geometrical non-linearity, expressing that the front tends to essentially propagate normally to itself.
- iii) The symbol CT stands for “counter terms”, that are present to ensure that front deformation field \mathcal{F} is “genuine”. It should not correspond to a (small) shift of the origin position, nor to a (small) shift of

the mean front radius. This property will be naturally enforced by cancelling the first coefficients of the Legendre-Fourier expansion of \mathcal{F} (see section 4.3).

- iv) The external forcing u' has to be prescribed and should mimic the effect of (weak) turbulence on the front. This shall be specified section 4.2.
- v) the coefficients $\Omega(\alpha)$ and $a(\alpha)$ (see also note ²) can be modified to meet asymptotic ($\alpha \rightarrow 0^+$) or linear limit behaviours. In the planar 2D case [30], they can also be tuned to quantitatively reproduce DNS results.

Equation (15) appears as simple³ and in a sense minimal in its structure — each building block has to be present to pertinently describe the physics. As mentioned above, and shown section 4.3, it is first-order in time, a quite clear (and simple) physical meaning can be associated to each present term⁴, and it is computationally easy to handle in the Fourier-Legendre spherical harmonics basis. Moreover, it is also robust against educated changes in the modelling [13]. As mentioned in the introduction, it requires few (3+turbulent forcing) and easy to change input parameters. Since it provides an equation for the whole deformed sphere — including the poles —, it has also been referred to as “accurate” in reference [43]⁵.

Note however that equation (15) needs be supplemented with an evolution equation for the mean surface [13] (i.e. here for the mean front radius R_M). In [29, 13], it is assumed that this mean radius evolves as

$$\frac{dR_M}{dt} = \frac{S_L^0}{1 - \alpha} \quad (16)$$

i.e. wrinkling does not affect flame propagation velocity. In most flamelet-based RANS or LES modelling [16], it is assumed that the effective turbulent consumption rate is proportional to the flame surface density or density of wrinkling (ibidem, eq. (5.4)). In the quasi-planar case, it can be asymptotically derived, for a large Zel’dovitch number and a unit Lewis number [30]), that for steady flame shapes the speed at which the front advances on average towards the fresh mixture is proportional to the flame surface increase. Using this argument, for large radii expanding flames⁶ (i.e $R_M \ll$ Markstein lengths), equation (16) can be combined with this quasi-planar limit to yield

$$\frac{dR_M}{dt} = \frac{S_L^0}{1 - \alpha} A_S \quad (17)$$

with $A_S = \frac{S(t)}{4\pi R^2}$ and $S(t)$ the actual flame surface area. Here, we are here interested in initially small radii flames (R_M ranging from 2 mm to 2 cm, to be compared with Markstein lengths $\sim 100 \mu\text{m}$), hence curvature and stretch effects are important at early times. Combining equations (17) — for large wrinkled expanding flames — and (10) — for laminar stretched flames, and $\xi = 2$ in the spherical case — we propose

$$\frac{dR_M}{dt} = \frac{S_L^0}{1 - \alpha} \cdot \frac{1}{1 + 2\mathcal{L}_b/R_M} \cdot A_S(t) \quad (18)$$

²Modifying $a(\alpha) > 1$ may also be a way of taking into account the influence of orthonormal velocity on non linear term [28]

³It is a differential-like equation in the Fourier-Legendre basis, even if the elliptic operator $H(\cdot)$ is non local in space.

⁴Of course, combustion physics is richer than that ! But, as this will be outlined in the paper, the main features will be captured by the modelling.

⁵This reference proposed an interesting Fourier-Fourier modeling on large equatorial sectors, but not including poles.

⁶Notice that the “large” flames we are interested in in the present paper are quite far away from a fractal behaviour ($R_M \sim t^\nu$, with $\nu \approx 1.5$) ; cf. e.g. [44].

as evolution equation for the mean flame front R_M . When $A_S \rightarrow 1$ (i.e. in absence of wrinkling), equation (18) yields (10), while when R_M is noticeably larger than \mathcal{L}_u (for larger radius flames), one gets equation (17).

The input parameters of the modelling are as follows : the density contrast α , the laminar flame velocity S_L^0 and the Markstein length \mathcal{L}_u . From these, one can deduce the neutral wavenumber K_n [45]

$$K_n = \frac{\alpha}{2(1-\alpha)\mathcal{L}_C} \simeq \frac{\alpha}{2(1-\alpha)\mathcal{L}_b} = \frac{\alpha}{2\mathcal{L}_u} \quad (19)$$

One should also provide an external forcing term u' , mimicking turbulence, that will be specified next subsection.

4.2. External forcing

To mimic the effect of turbulence on the front, an additive forcing u' (\sim the radial velocity component of the unburned mixture at the front) can be introduced. Since for weak turbulence, the flame acts as a band-pass filter for wave numbers (around $K = K_n$), a simple uncorrelated white noise would do the job [13, 45, 46, 36]. However, a more realistic turbulent forcing would be both correlated in space and time [29]. In the present study, since we wanted to compare EEM results with DNS and experiments, we made the EEM evolve in the same (statistically speaking) Passot-Pouquet “turbulent” flow as the one used to initialize turbulence in the DNS, possibly with the same or different random seeds used to generate it. To mimic turbulence temporal decay, we simply made the velocity components exponentially decrease with time, as it will be precised section 5. Notice that — at this stage — the modelling does not include flame retroaction on turbulence.

4.3. Numerical strategy

In the spectral Fourier-Legendre space, the evolution equation (15) can formally be cast as

$$\frac{\partial v_{lm}}{\partial t} = Lv_{lm} + N_{lm} \quad (20)$$

where L is a linear operator and N_{lm} denotes the Fourier-Legendre coefficient of the non linear term of (15), including the external forcing; v_{lm} denotes the $l - m$ coefficient (in the spherical harmonics basis Y_l^m) of \mathcal{F} (equation (15)) and

$$Lv_{lm} \equiv \frac{h(l)}{R_M} - \frac{1}{K_n} \frac{c(l)}{R_M^2}, \quad (21)$$

with

$$h(l) = 2l(l-1)/(2l+1) \quad (22)$$

and

$$c(l) = (l-1)(l+2) \quad (23)$$

as specified in reference [13]. As mentioned section 4.1 (item iii), the first terms are forced to zero ($v_{00} = v_{10} = v_{11} = 0$) to ensure “genuine” deformations only.

A quite convenient way to numerically solve equations of the same kind as (20) is to use Exponential Time Differencing Runge-Kutta (ETDRK) methods [47, 48, 49, 50]. If h denotes the (assumed constant) time step size, the first order and fourth order schemes [49] can respectively be written as

$$v_{n+1} = e^{Lh}v_n + \frac{e^{Lh} - 1}{L}N_n \quad (24)$$

and

$$a_n = v_n e^{Lh/2} + \frac{e^{Lh/2} - 1}{L} N_n, \quad N_a = N(a_n) \quad (25a)$$

$$b_n = v_n e^{Lh/2} + \frac{e^{Lh/2} - 1}{L} N_a, \quad N_b = N(b_n) \quad (25b)$$

$$c_n = a_n e^{Lh/2} + \frac{e^{Lh/2} - 1}{L} (2N_b - N_n), \quad N_c = N(c_n) \quad (25c)$$

$$\begin{aligned} v_{n+1} = v_n e^{Lh} &+ \frac{N_n}{L^3 h^2} (-4 - Lh + e^{Lh} (4 - 3Lh + L^2 h^2)) \\ &+ \frac{2(N_a + N_b)}{L^3 h^2} (2 + Lh + e^{Lh} (-2 + Lh)) \\ &+ \frac{N_c}{L^3 h^2} (-4 - 3Lh - L^2 h^2 + e^{Lh} (4 - Lh)) \end{aligned} \quad (25d)$$

When computing terms of the form $(e^z - 1)/z$ with $|z| \rightarrow 0$ numerical cancellation errors may lead to unacceptable inaccuracy or instability [49]. Following [49, 48], in order to avoid these errors for small values of $|Lh|$, the numerical evaluation of $(e^z - 1)/z$ makes use of a contour integral in the complex plane around $z = 0$. Preliminary tests on one-dimensional Michelson–Sivashinsky equation [21] showed it was more convenient to use the ETD4 method in terms of stability and CPU effort. Since we compare our EEM computation (less than 2 CPU hours) to heavier DNS computations ($\sim 70\,000$ CPU hours), we did not try to use fast and/or parallel spherical harmonics tools [51, 52]

In order to compare the EEM simulations with the DNS computations, we projected the velocity radial component from the 480^3 DNS grid ($\sim 100 \cdot 10^6$ points) to a coarser $100^3 = 10^6$ grid, in order to compute the input forcing u' to the EE. The EE is then solved on a Fourier-Legendre grid of 1313×1312 ($\approx 1.7 \cdot 10^6$) colocation points. For the 3 cm flame, the computational cost was a little more than 2 CPU hours on a 3 GHz Xeon processor.

5. Results and discussion

To reproduce an expanding stoichiometric propane/air flame at room pressure and temperature, the numerical value of the density contrast was taken as $\alpha = 0.85$.

For our 3D EEM simulation, the numerical value of the neutral wavenumber K_n is depending on the numerical values of the density contrast α and of the first Markstein length (equation (19)). To obtain a suitable numerical value for the Markstein length \mathcal{L}_u , we plot on figure 7 consumption velocity S_C (equation (3)) vs mean flame stretch k (equation (7)) for experimental results from [4] and from present DNS calculation. To get a consistent comparison, we performed some equatorial sections of the DNS profiles — as it is actually done in the experiments — and extract S_C and k from them. Table 2 gathers the obtained results, along with the deduced laminar flame velocity (value of S_C extrapolated at zero stretch). For our mixture, from literature, the unstretched laminar flame velocity is $S_L^0 = 0.407 \text{ m}\cdot\text{s}^{-1}$. In this turbulent case, these values are quite difficult to determine experimentally [16] and are subject to statistical variation. They indeed noticeably differ from one section (including experiment) to another. Still, the obtained results are compatible with the values determined in the laminar case (cf. table 1, $S_L^0 \approx 0.41 \text{ m}\cdot\text{s}^{-1}$ and $\mathcal{L}_u \approx 140 \mu\text{m}$), specifically for large radii (small values of k).

To take into account the temporal decay (with a characteristic time τ) of turbulence intensity, we multiplied the computed forcing u' by an exponential factor $e^{-t/\tau}$ with $\tau = 13 \text{ ms}$. This behavior was determined

Table 2: Determination of laminar flame velocity S_L^0 and of the first Markstein length \mathcal{L}_u from data of figure 7 .

Case	S_L^0 (cm/s)	\mathcal{L}_u (μm)
DNS cut (a)	44.7	154
DNS cut (b)	41.4	123
DNS cut (c)	39.3	107
Experiment [4]	35.9	107

from the (non reactive) isotropic turbulent flow simulation, used to initialize the flow before ignition. However, the presence of the flame modifies the turbulent flow, and this is not taken into account by the present EEM approach. As this will be presented subsection 5.1, a better agreement was obtained when decreasing the effective forcing felt by the flame by a factor $\beta = 0.6$. Combined with the turbulence decay rate, the actual forcing u'_a implemented in the simulation is $u'_a = u' \times \beta e^{-t/\tau}$. Moreover, in [29, 30], in the context of 2D planar flames, the coefficient $a(\alpha)$ in the Michelson-Sivashinsky equation (equivalent to the $a(\alpha)$ in equation (15) was tuned as a function of α in order to fit the front wrinkling amplitude and successfully reproduce DNS results.

To test the sensitivity of the results to the input parameters values — which are not precisely known —, we ran different EEM simulations by slightly changing some parameters around their nominal or assumed value. These parameters were respectively $a(\alpha)$ — appearing in equation (15) —, the Markstein length \mathcal{L}_u — linked to K_n via equation (19) — and u'/S_L — the effective intensity of the forcing felt by the flame, via the β parameter.

The original value for $a(\alpha)$ ($\equiv 2/(2 - \alpha) \simeq 1.739$ for $\alpha = 0.85$) was modified to its fitted value in the planar case from [29, 30] to give $a^{fit}(\alpha) \simeq 2.071$ for $\alpha = 0.85$.

The numerical value for \mathcal{L}_u was taken as 100, 120 and 138 μm respectively, since the measured values for this parameter show a quite important dispersion (as it is well known [16]) but still of the order of 100 μm . The β parameter was also tuned from 1.0 to 0.6. This parameter may be seen as a correction for retroaction effect of the flame on turbulence, which is not taken into account in the present approach. Indeed, a laminar expanding flame radius R essentially grows like $dR/dt = S_b = \rho_u S_L^0 / \rho_b$ (cf. equations (2) or (9)). Fixed vortices of size l would then be consumed in a time $\sim l/S_b$, whereas a real flame would consume them in a time $\sim l/S_L^0$ since gas expansion pushes away the vortices in the radial direction at a speed $S_b - S_L^0$. A way of taking into account gas expansion would be to elongate (of a factor ρ_u/ρ_b) in the radial direction the (non moving) vortices seen by the flame [29]. The intensity decrease of the synthetic forcing (via the β parameter) may constitute a simple way to take into account this ‘‘Doppler effect’’ on the flame propagation. In the context of the present paper, we did not attempt any change of modelling for the curvature and hydrodynamic operators expressions C and H (equations (22–23); see [13]).

To ensure the robustness of the approach to statistical variation, we also changed the random seed parameters (used by the pseudo-random numbers generator) for the initial Passot-Pouquet spectrum, corresponding to the four EEM samples in figures 12–16).

5.1. Comparison with DNS and experimental results

We quantitatively compared the results obtained with the EEM strategy to the outputs from experiments [4] and present DNS results (section 3).

Figures 12 show the results obtained with the a priori ‘‘nominal’’ values of the parameters — that are in fact somewhat arbitrary — corresponding to $\mathcal{L}_u = 138 \mu\text{m}$, $a(\alpha) = 2/(2 - \alpha) \simeq 1.74$ (from reference [13]) and $\beta = 1$. Figures 12–(a) to 12–(f) respectively show temporal evolution of radii R_P and R_S , mean stretch

k , consumption speed S_C and mean turbulent velocity S_T as functions of R_S , and S_C as a function of k . The results from the experiments (quoted as EXP) as those of [4]. The four equatorial sections from EEM are obtained thanks to four different random seeds for the passot-Pouquet spectrum. Results obtained by DNS refer to three different perpendicular sections of the 3D expanding simulation. While results between DNS and EXP are quite in line (except for difficult-to-determine outputs like S_C , S_T and k), results from EEM, even if compatible, are slightly shifted to higher values, indicating the external forcing felt by the flame may be too large.

To correct this too large “turbulence”, we decreased the β parameter (from 1. to 0.6). Similar results are presented on figures 13. Quite fair agreement is now obtained between EEM, DNS and EXP results, in particular at large radii and small stretch. Dispersion of results between the 3 sections of the (one-shot) DNS result is compatible with EXP and EEM results.

To check the robustness and well-posedness of the modelling — do small changes in the input parameters induce small changes in the outputs ? — we made some parameters vary. We first made vary the value of Markstein length \mathcal{L}_u , which is known to be difficult to determine [16], down to 120 and 100 μm . The results, similar to the one of figures 13 are shown figures 14 and 15. They indicate a quite low sensitivity of the results to this parameter and this may be seen as a comforting argument to the EEM approach, since

A CREUSER: OU ENTRE le L_U DANS LE MODELE...

As already mentioned, the coefficient $a(\alpha)$ was also increased to its “planar best-fit” value of 2.07 [30] for $\alpha = 0.85$, corresponding to equation (26):

$$a(\alpha) = 1 + \frac{1}{2}\alpha + \frac{3}{8}\alpha^2 + \frac{4}{3} \left((1 - \alpha)^{-1/4} - \left(1 + \frac{\alpha}{4} + \frac{5\alpha^2}{32} \right) \right) \quad (26)$$

The results, similar to the one of figures 13 are shown figures 16. We also tried to increase the value of a even more, up to the arbitrary value of 2.5, without noticing any qualitative change in the results. For the sake on brevity, these results are not shown here.

The value of Markstein length

The visual resemblance is striking

6. Concluding remarks, future work

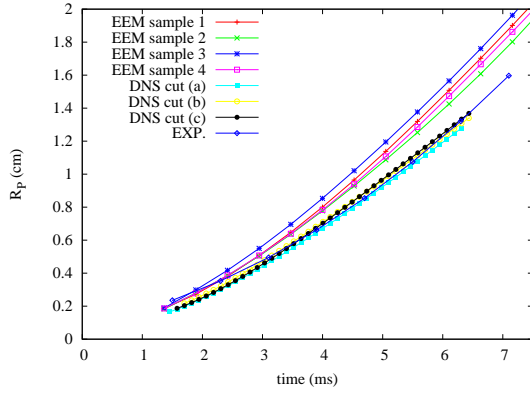
References

- [1] X. Gu, M. Haq, M. Lawes, R. Woolley, Laminar burning velocity and Markstein lengths of methane–air mixtures, *Combustion and flame* 121 (1-2) (2000) 41–58.
- [2] D. Bradley, R. Hicks, M. Lawes, C. Sheppard, R. Woolley, The measurement of laminar burning velocities and markstein numbers for iso-octane–air and iso-octane–n-heptane–air mixtures at elevated temperatures and pressures in an explosion bomb, *Combustion and flame* 115 (1) (1998) 126–144.
- [3] N. Peters, Laminar flamelet concepts in turbulent combustion, *Symposium (International) on Combustion* 21 (1) (1988) 1231 – 1250, 21st Symposium (International) on Combustion. doi:DOI: 10.1016/S0082-0784(88)80355-2.
- [4] B. Renou, Contribution à l’étude de la propagation d’une flamme de prémélange instationnaire dans un écoulement turbulent. Influence du nombre de Lewis., PhD thesis.
- [5] O. Pajot, Etude expérimentale de l’influence de l’aérodynamique sur le comportement et la structure du front de flamme dans les conditions d’un moteur à allumage commandé., PhD thesis.

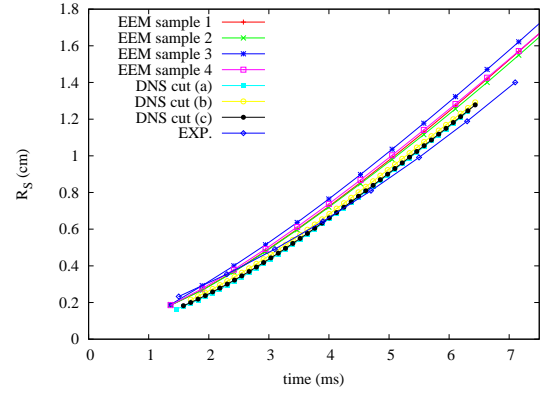
- [6] F. Foucher, Etude expérimentale de l'interaction flamme-paroi : Application au moteur à allumage commandé., PhD thesis.
- [7] F. Foucher, S. Burnel, C. Mounaïm-Rousselle, Evaluation of burning rates in the vicinity of the piston in a spark-ignition engine, *Proceedings of the Combustion Institute* 29 (1) (2002) 751–757.
- [8] B. Lecordier, Etude de l'interaction de la propagation d'une flamme prémélangée avec le champ aérodynamique par association de la tomographie laser et de la vélocimétrie par images de particules., PhD thesis.
- [9] G. Groot, L. De Goey, A computational study on propagating spherical and cylindrical premixed flames, *Proceedings of the Combustion Institute* 29 (2) (2002) 1445–1451.
- [10] G. Groot, Modelling of propagating spherical and cylindrical premixed flames., PhD thesis.
- [11] J. Oijen, R. Bastiaans, G. Groot, L. Goey, Direct numerical simulations of premixed turbulent flames with reduced chemistry: Validation and flamelet analysis, *Flow, Turbulence and Combustion* 75 (1) (2005) 67–84.
- [12] C. Altantzis, Numerical investigation of the dynamics of unstable lean premixed hydrogen/air flames, PhD thesis, ETHZ Zurich.
- [13] Y. D'Angelo, G. Joulin, G. Boury, On model evolution equations for the whole surface of three-dimensional expanding wrinkled premixed flames, *Combustion Theory and Modelling* 4 (3) (2000) 317–338.
- [14] B. Renou, A. Boukhalfa, D. Puechberty, M. Trinité, Local scalar flame properties of freely propagating premixed turbulent flames at various Lewis numbers, *Combustion and Flame* 123 (4) (2000) 507–521.
- [15] B. Renou, A. Boukhalfa, An experimental study of freely propagating premixed flames at various Lewis numbers, *Combustion Science and Technology* 16 (2001) 347–370.
- [16] T. Poinso, D. Veynante, *Theoretical and Numerical Combustion*, R.T. Edwards Inc., 2005.
- [17] F. Baillot, D. Durox, D. Demare, Experiments on imploding spherical flames: effects of curvature, *Proceedings of the Combustion Institute* 29 (2) (2002) 1453–1460.
- [18] F. Williams, A review of some theoretical considerations of turbulent flame structure, *AGARD Anal. and Numerical Methods for Invest. of Flow Fields with Chem. Reactions, Especially Related to Combust.* 25 p(SEE N 75-30359 21-31).
- [19] T. Tahtouh, F. Halter, C. Mounaïm-Rousselle, Measurement of laminar burning speeds and Markstein lengths using a novel methodology, *Combustion and Flame* 156 (9) (2009) 1735–1743.
- [20] L. Vervisch, B. Labégorre, J. Réveillon, Hydrogen–sulphur oxy-flame analysis and single-step flame tabulated chemistry, *Fuel* 83 (4-5) (2004) 605–614.
- [21] E. Albin, Contribution à la modélisation numérique des flammes turbulentes : comparaisons dns-eem-expériences., Ph D Thesis.

- [22] E. Albin, Y. D'Angelo, L. Vervisch, Using staggered grids with characteristic boundary conditions when solving compressible reactive navierstokes equations, *International Journal for Numerical Methods in Fluids* (2011) n/a–n/doi:10.1002/fld.2520.
URL <http://dx.doi.org/10.1002/fld.2520>
- [23] C. S. Yoo, H. G. Im, Characteristic boundary conditions for simulations of compressible reacting flows with multi-dimensional, viscous and reaction effects, *Combustion Theory and Modelling* 11 (2) (2007) 259–286.
- [24] T. Poinso, S. Lele, Boundary conditions for direct simulations of compressible viscous flows, *Journal of computational physics* 101 (1) (1992) 104–129.
- [25] G. Lodato, P. Domingo, L. Vervisch, Three-dimensional boundary conditions for direct and large-eddy simulation of compressible viscous flows, *Journal of Computational Physics* 227 (10) (2008) 5105–5143.
- [26] T. Passot, A. Pouquet, Numerical simulation of compressible homogeneous flows in the turbulent regime, *Journal of Fluid Mechanics* 181 (1987) 441–466. doi:10.1017/S0022112087002167.
- [27] G. Sivashinsky, Nonlinear analysis of hydrodynamic instability in laminar flames. I- Derivation of basic equations, *Acta Astronautica* 4 (1977) 1177–1206.
- [28] Sivashinsky, G.I., Clavin, P., On the nonlinear theory of hydrodynamic instability in flames, *J. Phys. France* 48 (2) (1987) 193–198. doi:10.1051/jphys:01987004802019300.
- [29] G. Boury, Etudes théoriques et numériques de fronts de flammes plissées : dynamiques non-linéaires libres ou bruitées., PhD thesis.
- [30] G. Boury, Y. D'Angelo, On third order density contrast expansion of the evolution equation for wrinkled unsteady premixed flames, *International Journal of Non-Linear Mechanics*doi:DOI:10.1016/j.ijnonlinmec.2011.05.018.
- [31] J. Dold, G. Joulin, An evolution equation modeling inversion of tulip flame, *Combustion and Flame* 100 (1995) 450–456.
- [32] R. Rego, On a non-linear model of flame/acoustics interaction, PhD thesis.
- [33] K. A. Kazakov, On-shell description of stationary flames, *Physics of Fluids* 17 (3) (2005) 032107. doi:DOI:10.1063/1.1864132.
- [34] H. El-Rabii, G. Joulin, K. A. Kazakov, Nonperturbative approach to the nonlinear dynamics of two-dimensional premixed flames, *Phys. Rev. Lett.* 100 (17) (2008) 174501. doi:10.1103/PhysRevLett.100.174501.
- [35] V. V. Bychkov, Nonlinear equation for a curved stationary flame and the flame velocity, *Physics of Fluids* 10 (8) (1998) 2091–2098. doi:DOI:10.1063/1.869723.
- [36] B. Denet, Sivashinsky equation in a rectangular domain, *Physical Review E* 75 (4) (2007) 46310.
- [37] V. Karlin, V. Maz'ya, G. Schmidt, High accuracy periodic solutions to the sivashinsky equation, *Journal of Computational Physics* 188 (1) (2003) 209 – 231.

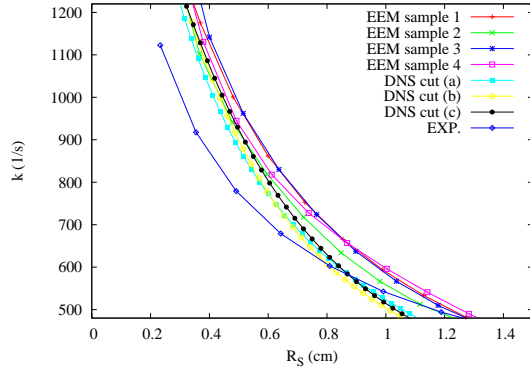
- [38] F. Creta, N. Fogla, M. Matalon, Turbulent propagation of premixed flames in the presence of darriuslandau instability, *Combustion Theory and Modelling* 15 (2) (2011) 267–298.
- [39] M. Frankel, An equation of surface dynamics modeling flame fronts as density discontinuities in potential flows, *Physics of Fluids A* 2 (10).
- [40] B. Denet, Frankel equation for turbulent flames in the presence of a hydrodynamic instability, *Phys. Rev. E* 55 (6) (1997) 6911–6916. doi:10.1103/PhysRevE.55.6911.
- [41] B. Denet, Nonlinear model equation for three-dimensional bunsen flames, *Physics of Fluids* 16 (4) (2004) 1149–1155.
- [42] V. Karlin, G. Sivashinsky, The rate of expansion of spherical flames, *Combustion Theory and Modelling* 10 (4) (2006) 625–637.
- [43] V. Karlin, G. Sivashinsky, Asymptotic modelling of self-acceleration of spherical flames, *Proceedings of the Combustion Institute* 31 (1) (2007) 1023 – 1030.
- [44] Y. Gostintsev, A. Istratov, Y. Shulenin, Self-similar propagation of a free turbulent flame in a mixed gaseous mixture, *Comb. Expl. Shock Waves* 24 (5) (1988) 63–70.
- [45] P. Cambray, K. Joulain, G. Joulin, Dynamique, propre ou bruitee, de flammes plissees en expansion, Unpublished DRET report 93 (1996) 060.
- [46] G. Joulin, G. Boury, P. Cambray, Y. D’Angelo, K. Joulain, Nonlinear dynamics of wrinkled premixed flames and related statistical problems, *Lecture Notes in Physics* (2001) 127–158.
- [47] S. Cox, P. Matthews, Exponential time differencing for stiff systems, *Journal of Computational Physics* 176 (2) (2002) 430–455.
- [48] Q. Du, W. Zhu, Analysis and applications of the exponential time differencing schemes and their contour integration modifications, *BIT Numerical Mathematics* 45 (2) (2005) 307–328.
- [49] A. Kassam, L. Trefethen, Fourth-order time-stepping for stiff PDEs, *SIAM Journal on Scientific Computing* 26 (4) (2005) 1214–1233.
- [50] P. Livermore, An implementation of the exponential time differencing scheme to the magnetohydrodynamic equations in a spherical shell, *Journal of Computational Physics* 220 (2) (2007) 824–838.
- [51] R. Stompor, S2hat parallel scalable spherical harmonic transform package.
URL <http://www.apc.univ-paris7.fr/~radek/s2hat.html>
- [52] C. Cantalupo, ccsht: A fast parallel spherical harmonic transform.
URL <http://crd.lbl.gov/~cmc/ccSHTlib/doc/index.html>



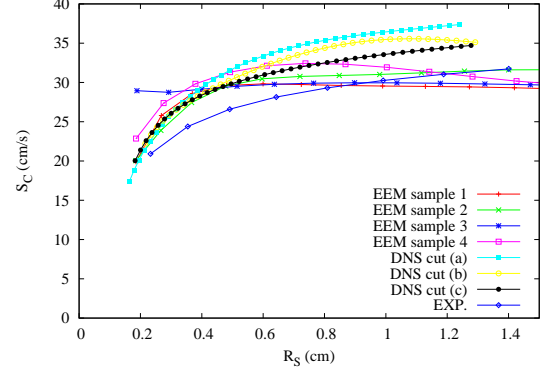
(a)



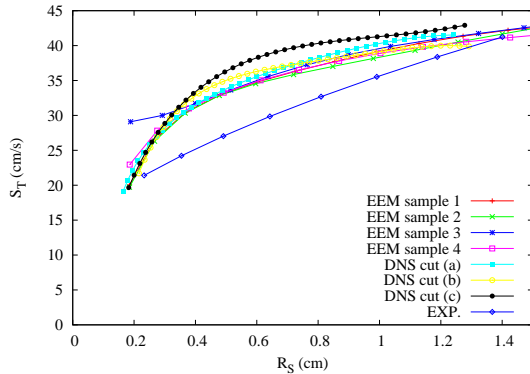
(b)



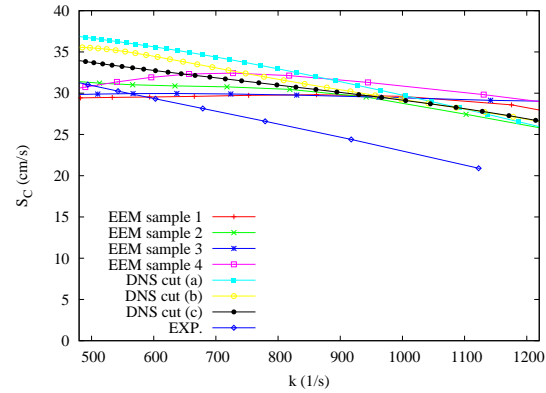
(c)



(d)

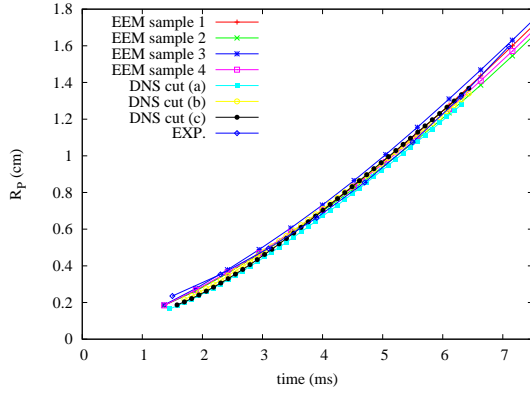


(e)

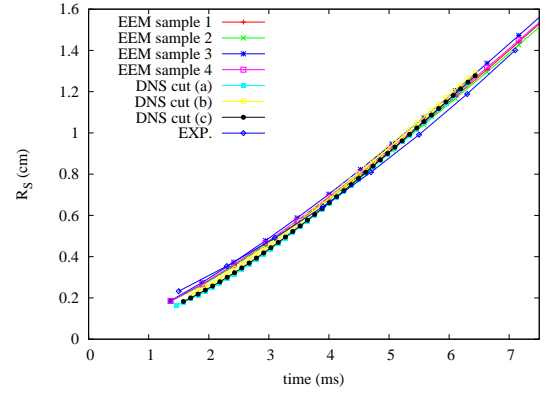


(f)

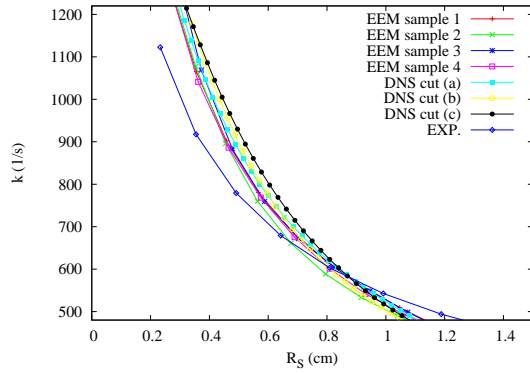
Figure 12: Comparison of DNS, EEM and experimental results from [4]. Time evolution of radii R_P (a) and R_S (b); evolution of stretch k (c), consumption speed S_C (d) and mean turbulent velocity S_T (e) as a function of R_S ; evolution of S_C as a function of k (f). The set of used input parameters is: $\mathcal{L}_i = 138\mu\text{m}$, $a(\alpha) = 2/(2 - \alpha) \approx 1.74$ (from reference [13], $\beta = 1$).



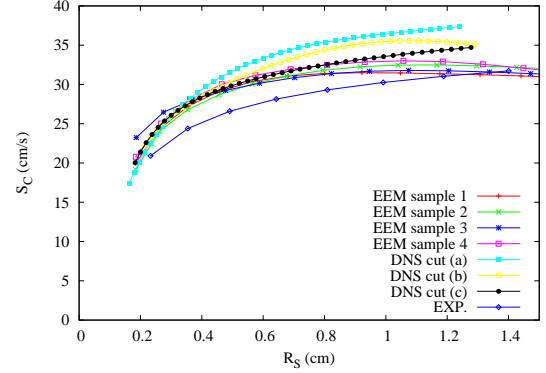
(a)



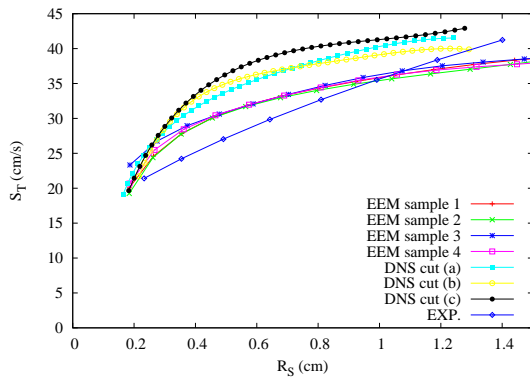
(b)



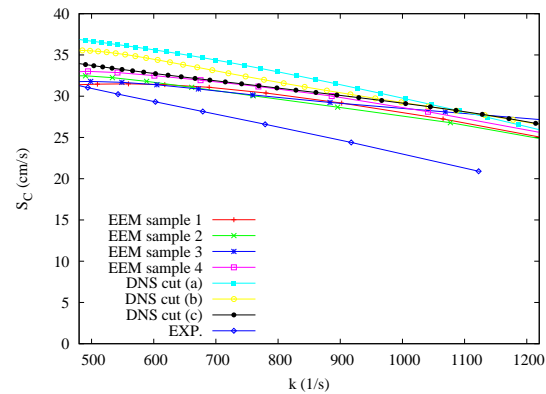
(c)



(d)

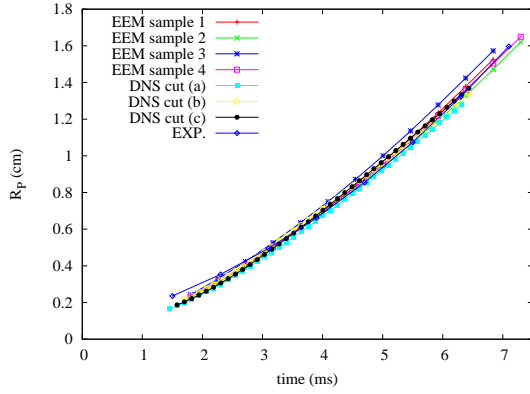


(e)

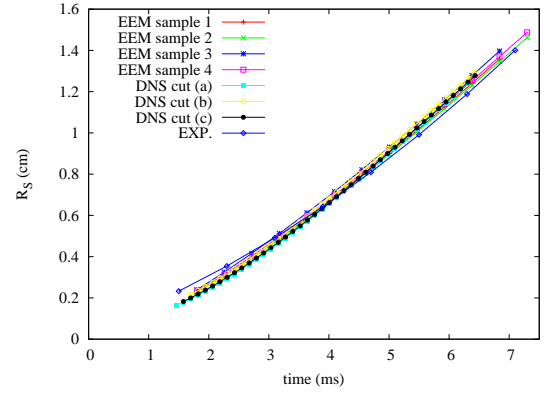


(f)

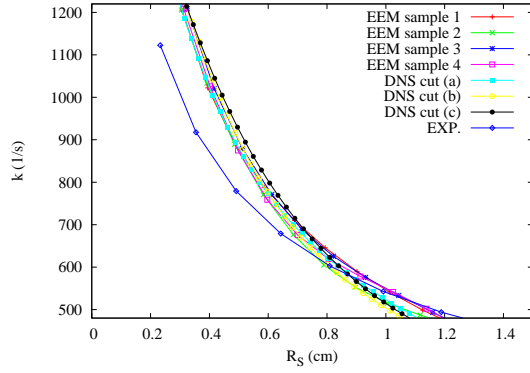
Figure 13: Comparison of DNS, EEM and experimental results from [4]. Time evolution of radii R_P (a) and R_S (b); evolution of stretch k (c), consumption speed S_C (d) and mean turbulent velocity S_T (e) as a function of R_S ; evolution of S_C as a function of k (f). The set of used input parameters is: $\mathcal{L}_i = 138\mu\text{m}$, $a(\alpha) = 2/(2 - \alpha) \approx 1.74$ and $\beta = 0.6$.



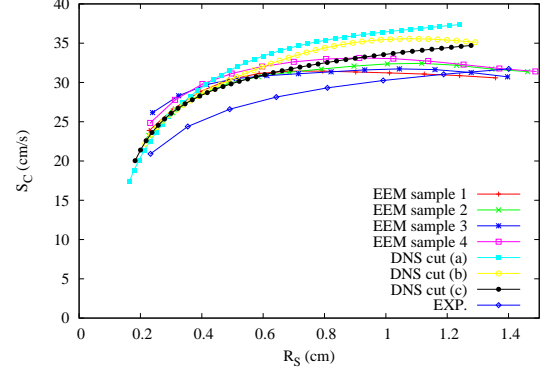
(a)



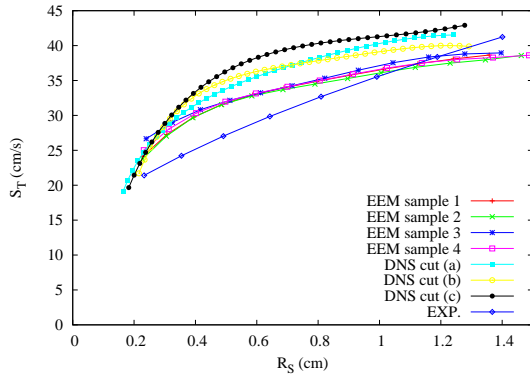
(b)



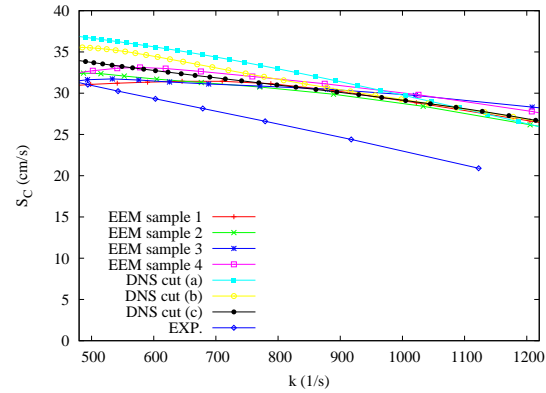
(c)



(d)

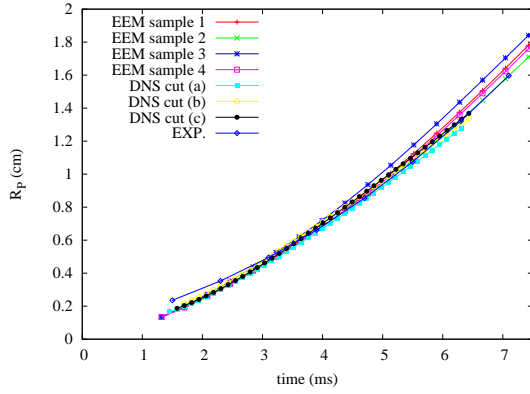


(e)

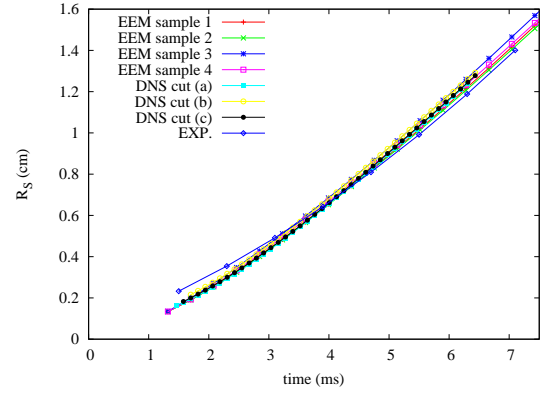


(f)

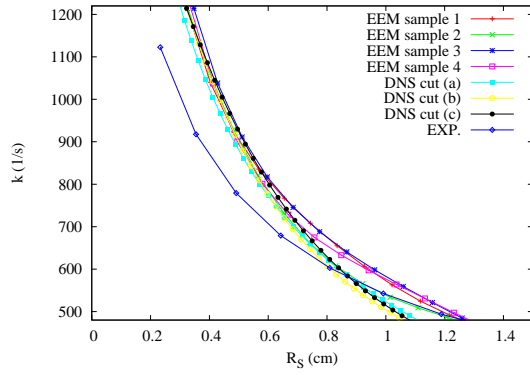
Figure 14: Comparison of DNS, EEM and experimental results from [4]. Time evolution of radii R_P (a) and R_S (b); evolution of stretch k (c), consumption speed S_C (d) and mean turbulent velocity S_T (e) as a function of R_S ; evolution of S_C as a function of k (f). The set of used input parameters is: $\mathcal{L}_i = 120\mu\text{m}$, $a(\alpha) = 2/(2 - \alpha) \approx 1.74$, $\beta = 0.6$.



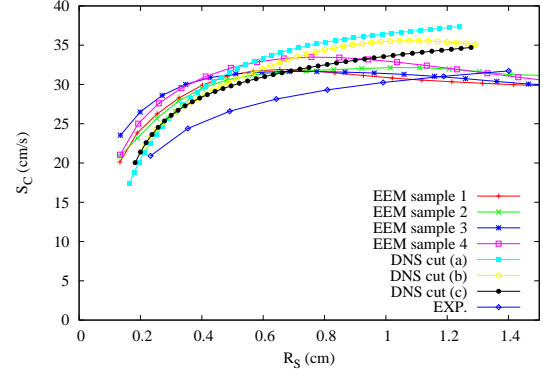
(a)



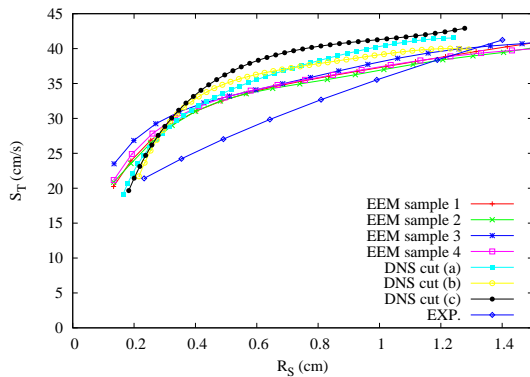
(b)



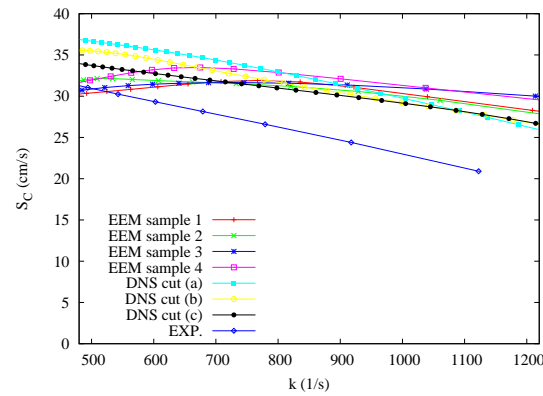
(c)



(d)

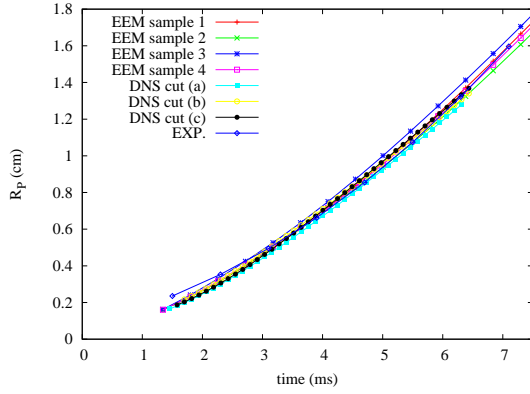


(e)

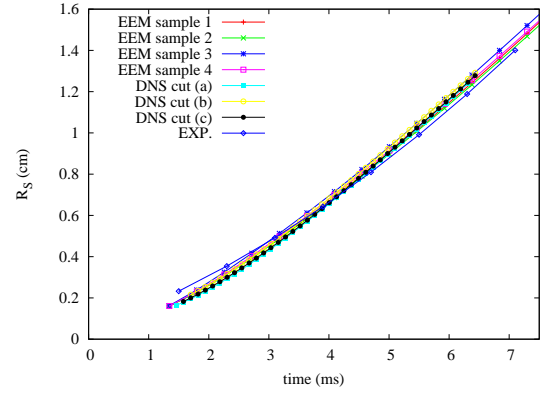


(f)

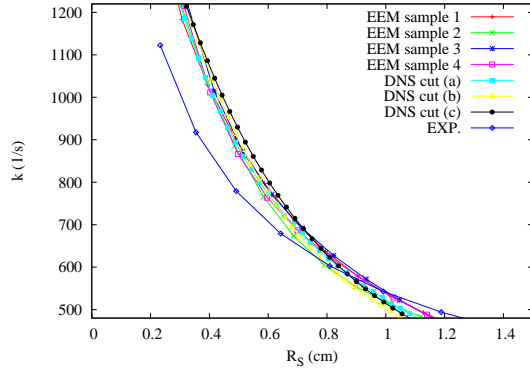
Figure 15: Comparison of DNS, EEM and experimental results from [4]. Time evolution of radii R_P (a) and R_S (b); evolution of stretch k (c), consumption speed S_C (d) and mean turbulent velocity S_T (e) as a function of R_S ; evolution of S_C as a function of k (f). The set of used input parameters is: $\mathcal{L}_i = 100\mu\text{m}$, $a(\alpha) = 2/(2 - \alpha) \approx 1.74$, $\beta = 0.6$.



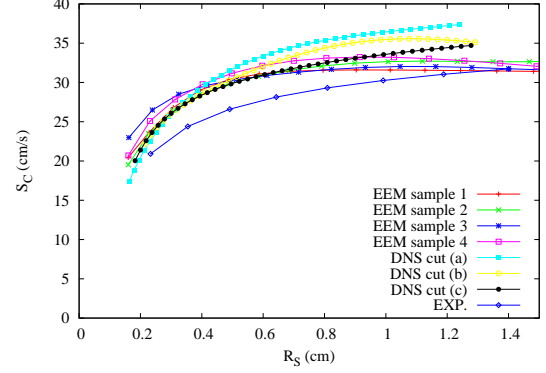
(a)



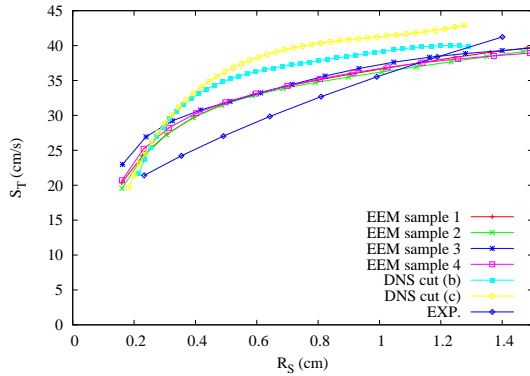
(b)



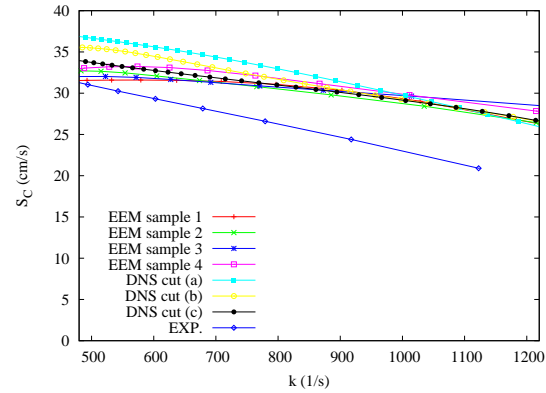
(c)



(d)



(e)



(f)

Figure 16: Comparison of DNS, EEM and experimental results from [4]. Time evolution of radii R_P (a) and R_S (b); evolution of stretch k (c), consumption speed S_C (d) and mean turbulent velocity S_T (e) as a function of R_S ; evolution of S_C as a function of k (f). The set of used input parameters is: $\mathcal{L}_i = 120\mu\text{m}$, $a(\alpha) \approx 2.07$ (best fit for planar flames, cf. [30]) and $\beta = 0.6$.

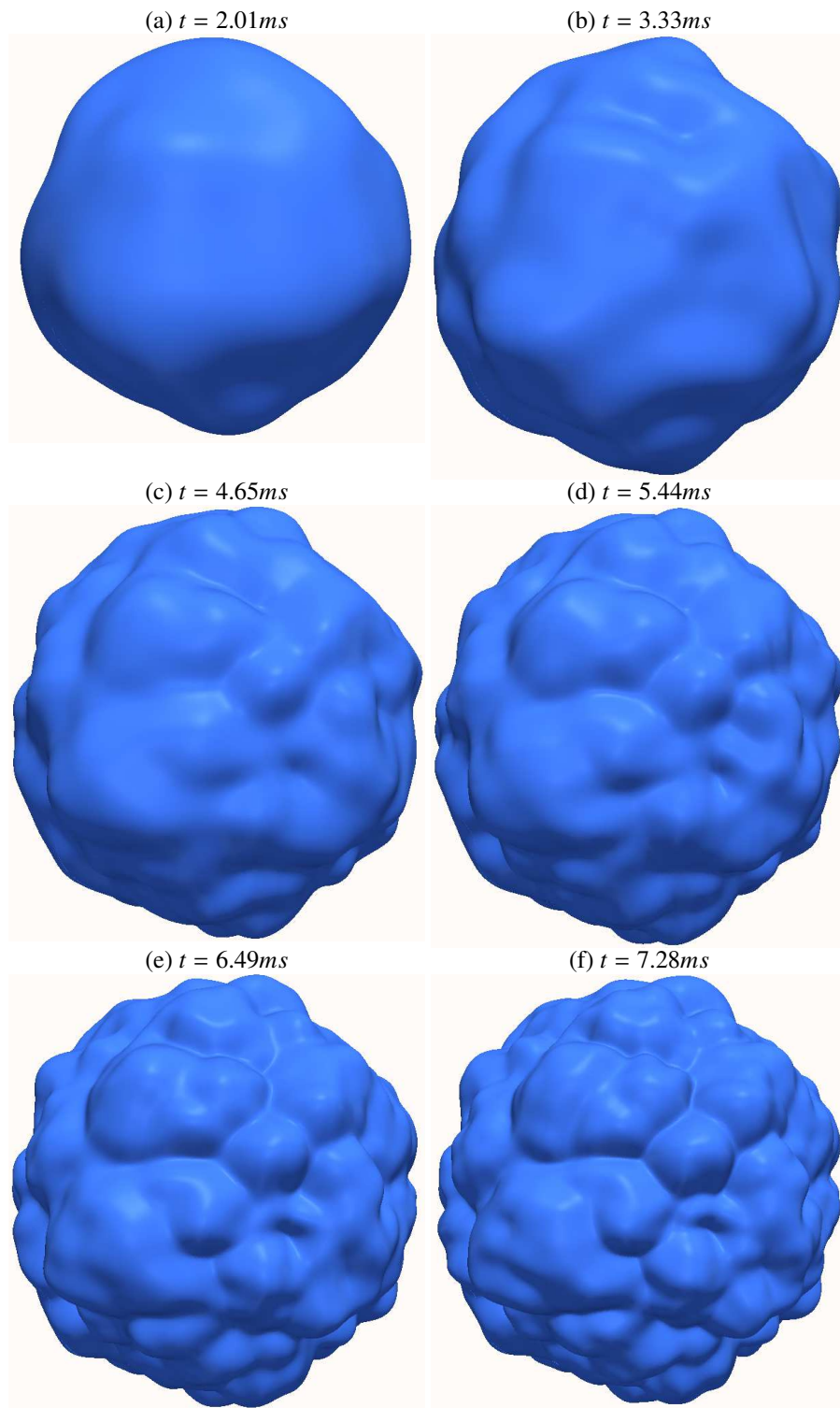


Figure 17: Sample numerical simulation of an expanding flame by the EEM approach. To ease readability, the mean radius has been re-scaled to max size for each figure. The corresponding times are respectively 2.01, 3.33, 4.65, 5.44, 6.49 and 7.28 ms. The corresponding mean radii are (in mm) 3.58, 6.26, 9.23, 11.1, 13.7 et 15.5. The set of used input parameters is : $\mathcal{L}_u = 138\mu\text{m}$, $a(\alpha) = 2/(2 - \alpha) \approx 1.74$ and $\beta = 0.6$. This figures are to be compared with the results from figures 9–10).

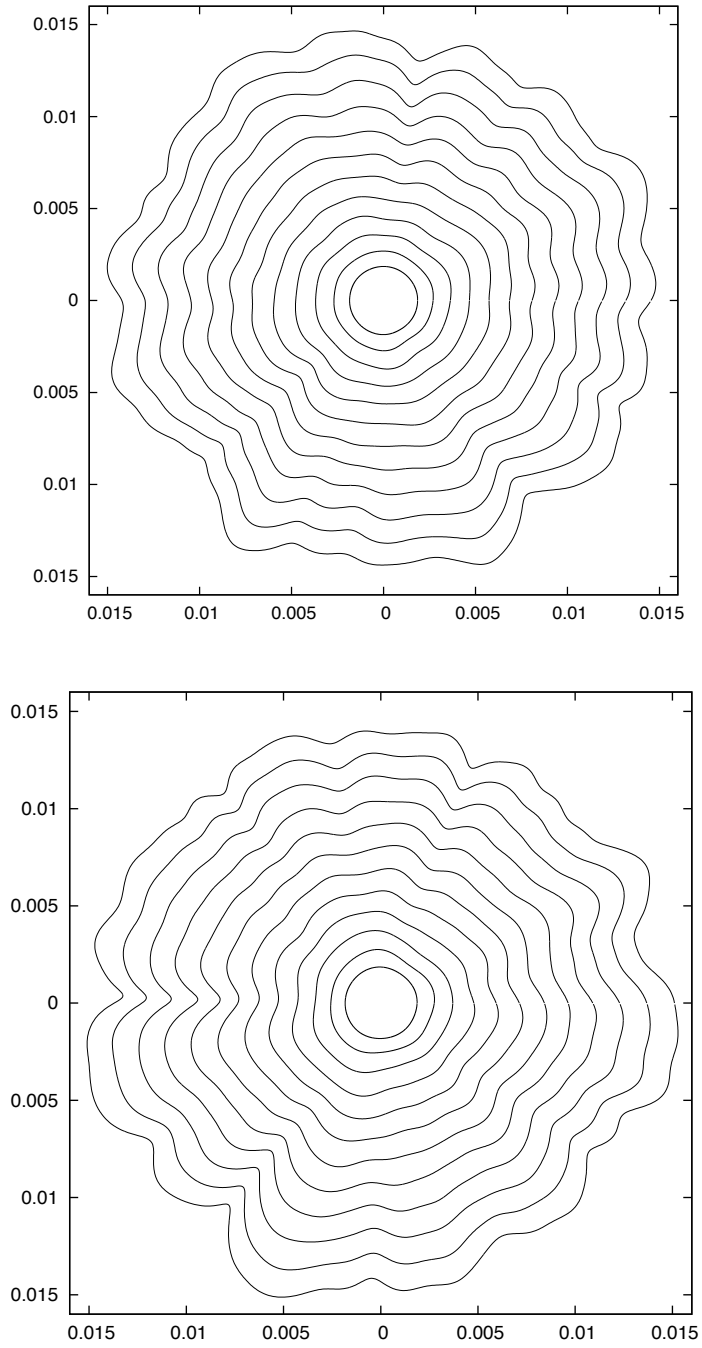


Figure 18: EEM strategy : two equatorial sections of the expanding front for two different realizations of Passot-Pouquet forcing (corresponding to samples 1 and 2 of figures 13) for $\mathcal{L}_H=138 \mu\text{m}$, $\beta = 0.6$ and $a = 1.74$. The time interval between two isolines is $\Delta t = 0.376\text{ms}$. These figures are to be compared with DNS results of figure 11.